

Spiral Arms In Gaseous Galactic Discs Driven By Different Mechanisms

A DISSERTATION PRESENTED
BY
YING ZHANG
TO
THE DEPARTMENT OF SCIENCE

IN PARTIAL FULFILLMENT OF THE REQUIREMENTS
FOR THE DEGREE OF
MASTER OF SCIENCE
IN THE SUBJECT OF
COSMOSCIENCES

HOKKAIDO UNIVERSITY
SAPPORO, HOKKAIDO
SEPTEMBER 2020

Spiral Arms In Gaseous Galactic Discs Driven By Different Mechanisms

ABSTRACT

Though various spiral structures and its formation mechanisms have been investigated since long before, but hardly gas dynamics had been compared between different candidate theories and particularly, spirals induced by triaxial dark halos is least learned. Peculiarly, whether triaxial dark matter halo could induce spirals in MW like galaxies and the gas response to halo perturbation still remains as a puzzle. In this thesis, we have implemented various galactic perturbations and performed simulations to investigate first, how gas disc responds to a adiabatically grown triaxiality of dark matter halo and second, comparing the dynamic responses of gas to different analytical galactic spiral perturbations in a MW like galaxy including density wave arms, dynamic arms, tidal interaction and triaxial dark matter halo. We found that triaxial dark matter halo does not necessarily induce spirals in gaseous galactic disc if its growth is adiabatic enough. Spirals induced by triaxial dark matter halo are very sensitive to the specific galaxy disc parameter, such as surface density distribution, rotation curve etc. An analysis of the azimuthal locations, the peaks in the velocity and density profiles show that different mechanisms contrast with each other in relationship of phase change in density, averaged azimuthal velocity and radial velocity , we then conclude it could be a diagnostic of the nature of spiral arms in real observed galaxies.

Contents

1	INTRODUCTION	1
1.1	Galaxy	1
1.1.1	Classification	1
1.1.2	Spiral Galaxies	4
1.1.3	Our Milky Way	8
1.2	Spiral Mechanisms	10
1.3	Motivation	14
1.3.1	Previous Studies On Dark Matter Halo Mechanism	14
1.3.2	Thesis Aim And Structure	15
2	METHODS	16
2.1	Code	16
2.2	Galactic Components	18
2.2.1	Initial Surface Density	18
2.2.2	Models	23
2.3	Perturbation Models	23
2.3.1	Quasi-stationary Arms	23
2.3.2	Dynamic Arms	26
2.3.3	Dark Matter Halo	27
2.3.4	Tidal Companion	31
3	RESULTS	33
3.1	Analysis Techniques	34
3.1.1	Gas Dynamics	34
3.1.2	Fourier Analysis	36
3.2	Dark Matter Halo	38
3.2.1	Low Resolution	38
3.2.2	Higher Resolution	39
3.3	Tidal Interaction	45
3.4	Density Wave and Dynamic Arms	49

4 CONCLUSION

52

REFERENCES

54

Listing of figures

1.1	Hubble tuning fork diagram	3
1.2	Observed rotation curve of Milky Way galaxy	5
1.3	Examples of grand and flocculent spirals in observed galaxies	7
1.4	Milky Way Galaxy	8
1.5	Epicycle orbits.	10
1.6	Spurs in global model.	13
1.7	Rotation speeds for a Milky Way-like rotation curve.	14
2.1	Initial surface density distribution	19
2.2	Initial particle distribution.	21
2.3	Disc rotation curve.	22
2.4	Initial surface density distribution curve.	24
2.5	Potential contour plot of dynamic arm potential before its peak.	26
2.6	Potential contour plot of dynamic arm potential after its peak.	27
2.7	Potential contour plot of triaxial dark matter halo perturbation.	29
2.8	Halo activation functions.	30
2.9	Potential contour plot of tidal interaction.	31
3.1	logged- $r - \theta$ map example.	35
3.2	Offset diagram example.	37
3.3	Summary of simulation results for triaxial dark matter halo perturbation with low resolution.	39
3.4	Triaxial Halo.	41
3.5	Logged $r - \theta$ density map of simulated triaxial dark matter halo on disc with flat rotation curve.	42
3.6	Density map of simulated triaxial halo impacts on a bulge-free disc.	43
3.7	Logged $r - \theta$ density map of triaxial dark matter halo perturbation.	44
3.8	Offset diagram of simulated triaxial dark matter halo perturbation.	45
3.9	Density map of simulated tidal interaction.	46
3.10	Logged $r - \theta$ density map of simulated tidal interaction.	47
3.11	Offset diagram of tidal interaction	48

3.12	Density map of simulated density wave arms and dynamic arms	50
3.13	logged $r - \theta$ density map of density wave arms and dynamic arms	50
3.14	Offset diagram of density wave arms and dynamic arms	51

Acknowledgments

I would like to thank the following people, without whom I would not have been able to complete this thesis. My supervisor Alex, for his enthusiasm for the project, for his guidance and patience. Particularly, his supervising style allowing me to explore many things turns me from studying to survive into enjoying learning. Thanks to Zhiqing, Nirmit, Elizabeth, Xuemei, Keying, truly great friends giving me tons of nice tips and hilarious jokes, thanks for all the caring during the two years. Thanks to my great best friend in college, Mingwei. I could not imagine what I would probably end up with without video chatting and studying with her everyday during this covid-19 pandemic though there's seven-hour time difference between us. Thanks to my parents, for their tolerance to a rebellious daughter who is also a heavy financial burden, for all their touching jokes, for sharing my dreams. In the end, I want to thank myself for not screwing up.

1

Introduction

1.1 GALAXY

1.1.1 CLASSIFICATION

Understanding the actual shape of the object where we stand on is already expensive either on a historical or cultural view, let alone the journey of exploring what about even outside the planet earth and our position within it.

Many talented astronomers have contributed in the process of mankind coming to realize that we are not alone in the universe or even just a little fish in a big pond.

Refractor-based extensive photographic survey enables scientists to conduct reliable separations of galaxies into classes. American astronomer Edwin Hubble established a crude but still nowadays widely-used classification scheme of galaxies in 1926 named as Hubble tuning fork diagram also known as Hubble sequence¹.

According to the original Hubble tuning fork diagram, galaxies can be categorized into Ellipticals and Spirals. Fig. 1.1 is a visualized figure to display the classification scheme. E stands for elliptical which is followed by a number from 1 to 7 so as to identify how much elliptical the galaxy is. Spirals galaxies noted as S are diverted from So class into two paths according to whether or not a notable bar-like structure appears in the central galaxy. Letters from a to c then further subdivide bar-free spiral galaxies into three groups in accordance with how compact their spirals are. Same thing for barred spiral galaxies expect they have a B in the classification to indicate bar structures. Spiral galaxies are usually flat disc-shaped and the tightness with which the spirals are wound partially depends on the bulge within the central disc. When the bulge dominates the galaxy a transition stage where builds the bridge between ellipticals and spirals come along and be classified as So also referred as Lenticular².

Elliptical galaxies surrounded by large amount of globular clusters envelope old light stars and sparse interstellar medium which suggests a low rate of star formation and shallow lightness. Stars in spiral galaxies are much younger than those found in Ellipticals. Spirals that take up two thirds of all galaxies usually indicate a rotationally symmetric, through which the galaxy could maintain its stability in order to fight against the self-gravitation. Structures such as bar and spiral arms within spiral galaxies are some of the most intriguing part in astronomy since they bring up star formation. There are also galaxies that neither showing a strong bulge more symmetric structures and then be pushed into a category called irregulars. Though the diagram is panelled from left to right, it is not

Edwin Hubble's Classification Scheme

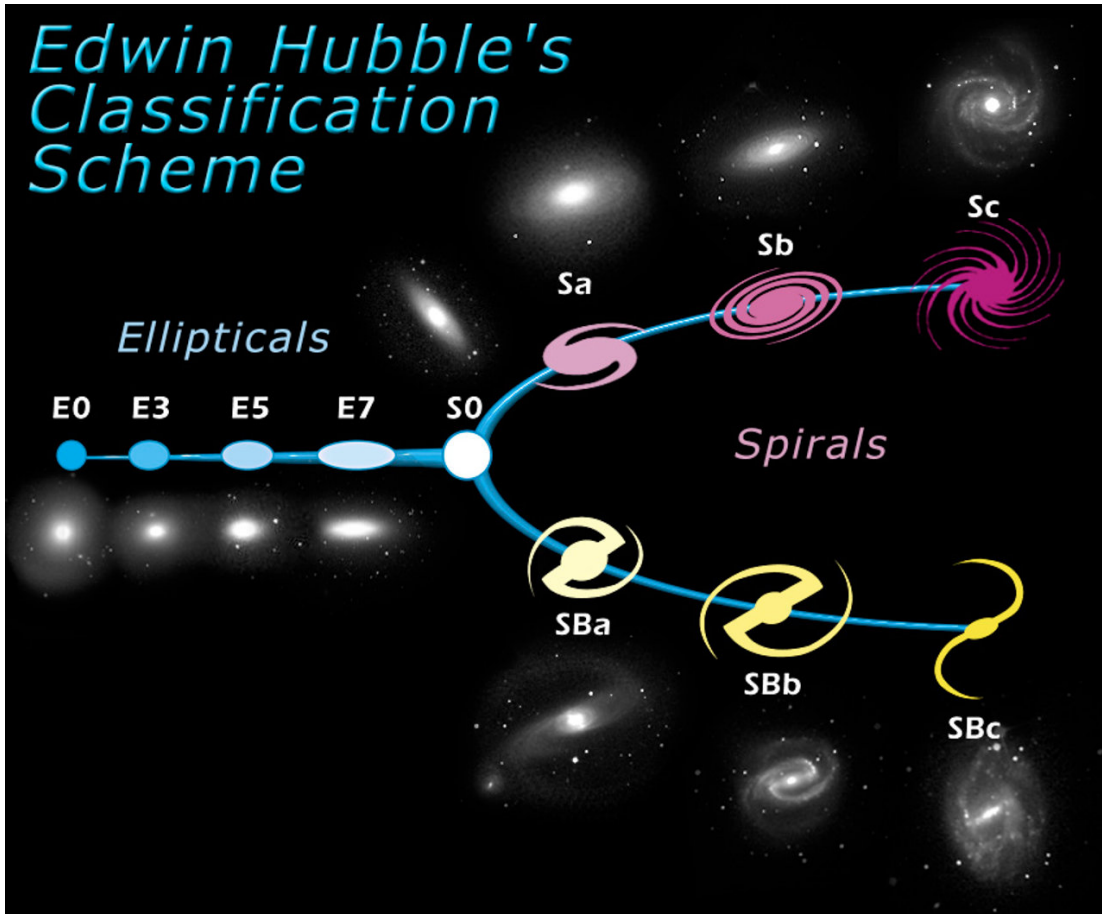


Figure 1.1: Hubble tuning fork diagram.

Adapted from <http://www.spacetelescope.org/images/heic9902o/> (credit: NASA and ESA).

considered as an evolutionary sequence of galaxies³.

Ellipticals, Spirals and Irregulars are those three classes that compose the modern Hubble tuning fork diagram, though the concept was later found to be an over-simplification. Galaxy evolution is a far more complex process than the illustrated diagram².

1.1.2 SPIRAL GALAXIES

In this thesis, we focus on spiral galaxies which are mainly rotationally supported by thin disks consisting of stars, gas and dust. In our universe, approximately two thirds of galaxies are spiral galaxies and around 60% of them exhibit grand design structure. Spiral galaxies often contain spiral arms together with bar-like structures, bulges and black holes in the inner region⁴. The most ideal resources for astronomical observation are those disk galaxies showing an edge-on view, which enables astronomers to reveal its vertical structures such as two separate disk components, a thin disk and a thick disk or spheroids. Studies of edge-on disk galaxies demonstrate most of the luminosity originates from the thinner disk. Here we briefly present some features of spiral galaxies.

Spiral galaxies usually have exponential luminosity profiles $I(r)$ where I_0 is a constant, r is the distance to disc center and b is a scale length.

$$I(r) = I_0 \exp(-r/b) \quad (1.1)$$

However, optical observations show that at small radii, luminosity profiles tend to deviate either above or below the exponential law and at large radii, the surface brightness could fall rapidly due to the truncation of galactic discs. Combining those results, a prevalent fitting function for 3D luminosity distribution of disks of spiral galaxies could be obtained. Notice though the vertical fitting function is established on theoretical basis, the radial fitting function is actually empirical and verified over a small range of surface brightness⁵.

As mentioned before, the stability of the galactic disk relies on the support from nearly circular rotation of stars and cold gas. Then the kinematic feature of the disk can be identified by rotation curve $V_{rot}(r)$. The rotational speed of massive galaxies typically rise rapidly at small radii and then keep extending flat shape. While dwarf and lower surface brightness systems commonly show slower central rises. Characteristics of rotation curves are often associated with disk structures such as bars

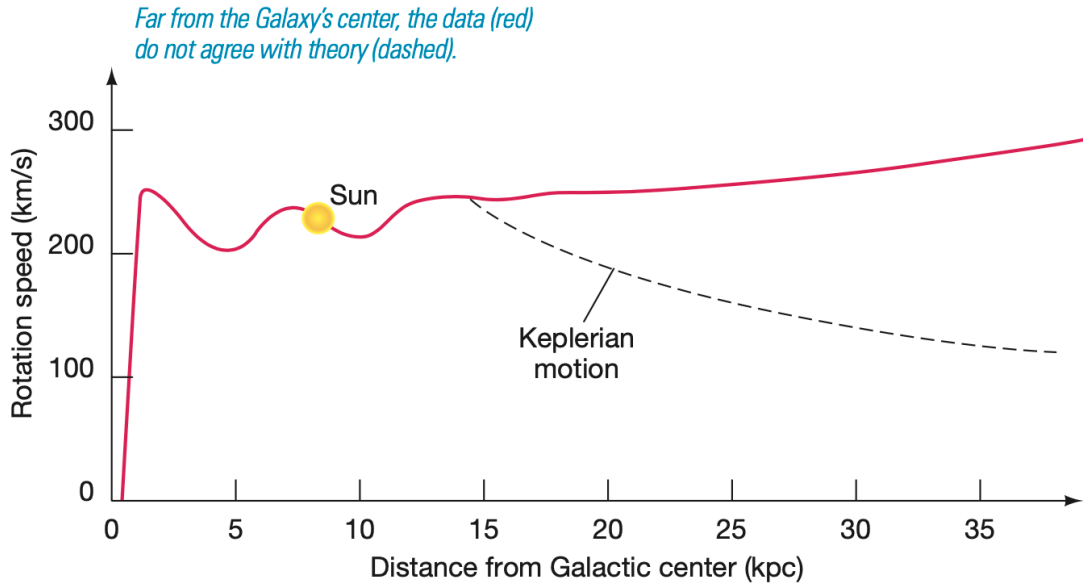


Figure 1.2: The rotation curve of Milky Way Galaxy.

Adapted from Astronomy Today Chap23⁶.

or spiral arms, though it is heavily system-by-system dependent⁶. The rotation curve is also a direct measure of the gravitational force within a disk and is given by

$$V_c^2(R) = \frac{Rd\Phi}{dR} \quad (1.2)$$

where r is the distance to central disc, G is the gravitational constant, and V_{rot} is the orbital velocity. Note that this is a more general definition, for a spherically symmetric potential, the right part of equation (1.2) could be replaced by $GM(R)/R$.

The rotational curves of galaxies are not linearly steep but instead, a flat curve as shown by fig. 1.2 demonstrating the rotation curve of our MW galaxy. This, on one hand, indicates that disk galaxies do not rotate as a rigid body, on the other hand, suggests that inner patterns revolve at a higher rotational speed so as to catch up with the outer patterns. After a few galactic rotations, as the stars and

gas closer to the center rotate faster than those at the edge of the disk, we could observe spirals wrap up, which is an effect called winding problem. This would cause us unlikely to observe any spirals in nature. Thus, the appearance of spirals indicates that its pattern speed may not rotate as the same speed as that of disc⁷.

On a large scale, stars and clouds in the disk rotates circularly around the galactic center in a differential manner. Some regions of the Galaxy are approaching the Sun, whereas others are receding from us⁶. The orbital speed in the vicinity of the sun is roundly 220km/s⁵. In contrast, motions of stars and gas galactic halo and bulge are more random and their trajectories satisfy a three-dimensional volume rather than on the plane of the disc, in other words, halo stars would penetrate in and out the disk. However, because individual star is hugely distant from one another and filled with interstellar medium between them, orbits of halo stars normally do not collide with disk stars. Interestingly, halo stars carries on some net rotation about the galactic center. In the light of radio observations, astronomers can measure the orbital motion of distant stars and gas and draw a curve known as rotation curve to obtain some critical features of galaxies⁶. Going contrast with the prediction from Newton's law, a falling off of orbital speed does not come to sight but instead, rises slightly and keeps flat extending out to a distance that reaches our measurement capabilities. The predicted amount of mass within 40kpc according to the Kepler equation

$$M(r \leq r_0) = r_0^3/T^2 \quad (1.3)$$

cannot support a rotation curve shaped like this, which indicates the disk luminous region is surrounded by an extensive, invisible three-dimensional dark halo that are invisible to all wavelengths. Moreover, dark matter halo even approximately occupies two-thirds if the MW's total mass inside the luminous area. Many candidates have been put up by Physicists to reveal the nature of dark matter halo, which hardly falls within the scope of this thesis.



Figure 1.3: Left is galaxy M51 showing grand-designed spirals. Right is galaxy NGC4414 displaying flocculent arms. Both are adapted from NASA.

Spirals typically display two systems according to their structures, one is grand-designed system whose arms usually extend out to the peripheral edge of the disk. This system sometimes involves with a strong bar or interaction with its neighbor. Another type of spirals care flocculent systems containing many arm segments and no apparent large-scale patterns. Fig 1.3 demonstrates grand-designed and flocculent arms. In terms of the rotation relativity, arms then could be classified into two types, leading and trailing arms. Leading arms refer to the direction of spiral winds pointing from the inner to outer of the disk is exactly the direction how gas particles and stars rotates within the disk. Most spiral galaxies show trailing arms instead of leading⁴.

Neutral hydrogen (HI) and molecular hydrogen (H_2) are the two major gas components disk galaxies, which differs form elliptical galaxies that manly contains gas in hot and highly ionized state³. Molecular gas, tracing the stars and often in the form of rings of dense gas, are detected via transition of CO. It is more concentrated in the central galaxy. CO emission goes hand in hand with occurrence of star formation and spiral structures. Late-type spirals show more gas fraction compared with early-type. However, a higher fraction of molecular gas appear in early-type galaxies while atomic gas dominates in late-type systems⁶. Low mass and low surfaces brightness galaxies

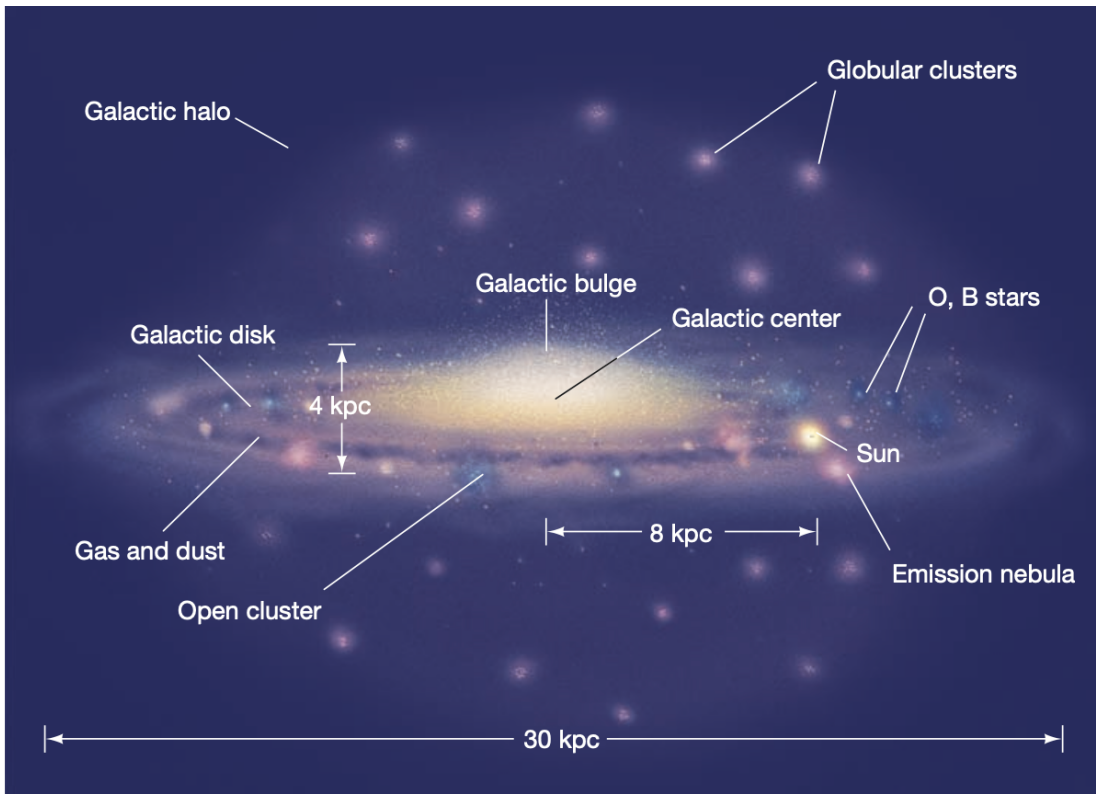


Figure 1.4: Milky Way Galaxy.

Adapted from Astronomy Today Chap23⁶.

usually inhabit a gas mass ratio of 80% while that of the massive spiral galaxies is 5%. Generally, the distribution of HI is the most extended³.

1.1.3 OUR MILKY WAY

The disk galaxy that we habit is known as Milky Way Galaxy (thereafter MW). Studying the MW often guide astronomers to compare with more distant and easily observable systems. Our MW is composed of galactic bulge, disk and halo. Galactic bulge located right in the center of disk together with galactic disk itself embeds in an approximately spherical ball named as galactic halo. Unlike the disk and bulge, the galactic halo barely contains gas or dust. Stars inhabit in bulge and halo regions

are identified distinctively redder than those are probed in the disk. Though those cooler red stars are actually relatively uniformly allotted around the disk, halo and bulge, hotter blue stars particularly live within the disk where active star formation happens. This difference marks that all the stars in the galactic halo are old and star formation within this region ceased for a long time due to a lack of gas and dust. On the other hand, galactic bulge demonstrates a high density of gas, contributing to a vigorous star formation site⁶.

Astronomers can measure the distance of a star from central disk by inferring its luminosity if it is recognized as a RR Lyrae or Cepheid type, which is also known as variable stars. Many RR Lyrae variables are found in globular clusters. Harlow Shapley states two crucial discoveries according to the observations of variable stars. First is most of the globular clusters reside at great distances, far away from the Sun. Second is he mapped the three-dimensional distribution of globular clusters and pointed out that those clusters extend 30 kpc across and roughly build up a spherical galactic system. He also demonstrated that we are not at the center of the MW but instead, 8 kpc away from the center⁶.

Optical techniques can only cover a small range of the galactic disk when astronomers work on to illustrate the different spatial distributions of galaxy matters because of the interstellar absorption. This leads to most of large scale observations rely on radio observations, especially 21-cm radio emission line generated by atomic hydrogen. Though radio-emitting gas exists out to over 50 kpc, both of stars and gas in the disk become sparse rapidly beyond around 15 kpc from the central galaxy⁵.

As a matter of fact, the abundance of stars above and below the disk plane would slowly increase, this is because near-planed-disk stars formed out of interstellar medium have a tendency to drift out of the disk over time because of interactions with nearby stars and molecular clouds. Nevertheless, the star motion in thick disk , which is an intermediate category between the older galactic halo and the younger disk, of MW can not be explained by the slow drift theory due to its great thickness, around 2-3 kpc. As for the galactic bulge, astronomers speculate the central part of our galaxy as

elongated, bar-like structure via observations of long wavelength⁶.

Interstellar gas in the galactic disk displays a defined pattern on a grand scale, which is known as spiral structure. Not only just interstellar gas and dust are found spiral arm patterned but also the young stellar and prestellar objects. The intriguing finding is spiral arm region is where star formation takes place and coherently, those bright young stellar matter can be easily seen in arm area even from far⁴. There are several different theories to address the origin, formation and dynamics of the spiral pattern, which we would introduce and discuss later in this thesis. Moreover, we focus on the gas spirals here and leave aside the stellar components.

1.2 SPIRAL MECHANISMS

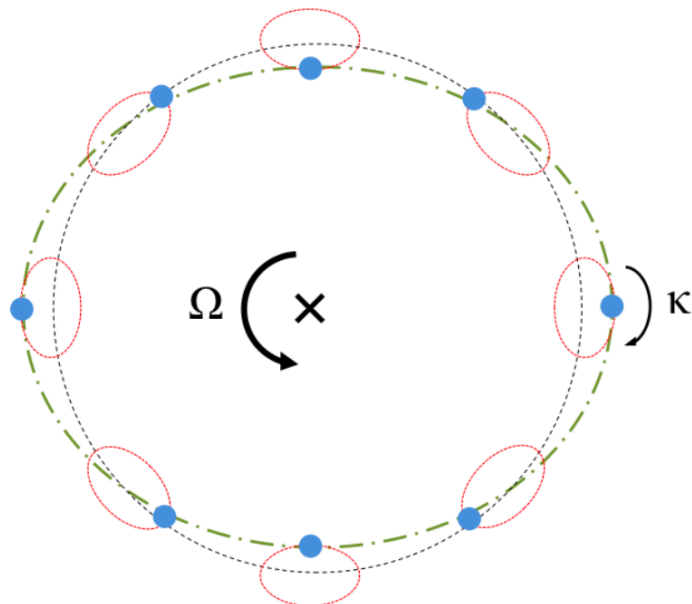


Figure 1.5: The orbital path of a star (blue dot) around the galactic centre with epicycle frequency of $\kappa = 2\Omega$. Red, black and green lines represent the epicycle, circular and resulting full orbital path respectively.
Adapted from A.R. Pettitt PhD thesis (2014) Figure 1.8.

Why would galaxies display such spiral structures at all and what is the physics behind this phenomena? Due to the interactions between stellar and gaseous component as they orbit around the galactic center, spiral structures could be induced according to the theory developed by Lindblad⁸. Consider aside from moving in a nearly-circular orbit, stars and gas in the disc also face a perturbation which absorbs both radial and azimuthal terms. (mathematical derivation given in appendix A.) In this case, star also rotates with a radial frequency of κ dependent on the rotation curve of the disc in the rotating reference. The mathematical relation is given below⁴.

$$\kappa^2 = R \frac{d\Omega^2}{dR} + 4\Omega^2 \quad (1.4)$$

where Ω is the orbital speed, R is the radius of the star. Since in inner disc where the rotation curve shapes like a rigid body and displays a flat shape in outer regions, this indicates stars moves around a elliptical path instead of nearly-circle in inner disc and also they finish their epicycle movement before completing a circular orbit around the central disc.

Thereafter, there are various theories of mechanisms developed trying to decipher the mechanisms behind the galactic spirals. In this thesis, we focus on the quasi-stationary density wave theory, dynamic arms, tidal interaction and triaxial dark matter halos. Gas and stars respond to galactic spirals in quite different ways because velocity dispersion of gas is much smaller compared with that of stars, which allows us to observe conspicuous arm structures in the disc. Furthermore, overdensities of gas also indicate possible sites of the recent star formation⁴. In this thesis, we keep a focus on the gas response to induced spirals.

Density wave theory presents that spirals display a fixed pattern speed. Different from material arms demonstrating a coronation between gas, stars and spirals everywhere in the disc, this quasi-stationary arm theory states spirals are not material but instead, resemble traffic roads in real world. Gas and disc slow down their rotational speeds as they enter the traffic area which is the spiral here

and speed up again as they leave. According to the resulting relation of dispersion relation of this theory, a physics parameter referred as Toomre Q could be calculated to indicate the balance between the bounding gravitational force and disc pressure force exerted on gas particles⁴.

$$(\omega - m\Omega)^2 = \kappa^2 - 2\pi G\Sigma \quad (1.5)$$

where k , ω and Σ are the radial wavenumber of the density wave, its angular frequency and surface density respectively.

$$Q_g = \frac{\kappa c_s}{\pi G\Sigma} \quad (1.6)$$

where κ , c_s , and G represent the elliptical frequency, sound speed, gravitational constant respectively. $Q_g > 1$ must be satisfied when the gas disc is stable. The rotation speeds for a MW like galaxy is shown by Fig. 1.7 and when material moves at the same orbital speed as the spiral density wave, this special situation is called co-rotation (thereafter CR). Inner Lindblad resonance (there after ILR) refers to material orbits faster than the spiral pattern and the opposite case is then be named as outer Lindblad resonance (thereafter OLR). The plot indicates density wave theory could allow induced arms to wind up as it transits to a loose leading wave, which goes against the requisite of rigid rotation for the spital perturbation.

Large-scale shocks are predicted by the density wave theory since gas would experience a sudden drop in velocity as they enter the spiral and speed up as they leave. This provides possibilities for star formation and together with cooling, this could also form substructures like spurs⁹ shown in Fig. 1.6 along the spirals.

Different from what quasi-stationary density wave theory proposes, spirals are usually observed as transient in N-body simulations. Swing amplification is the major mechanism to generate such featured spirals. In dynamic spirals, gas corresponds to the gravitational potential of arms and in

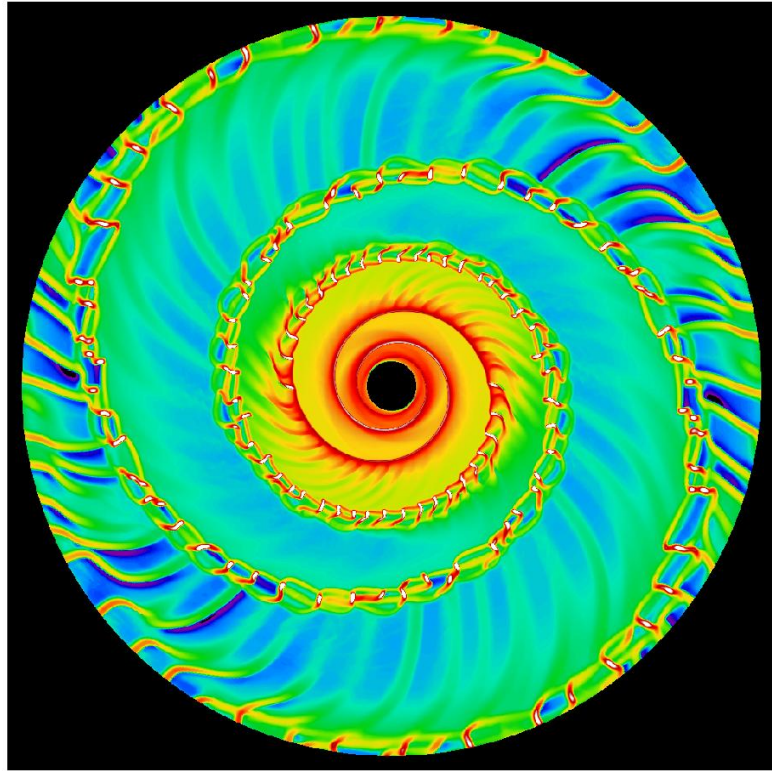


Figure 1.6: Snapshot from global model, after gas has collapsed into giant clouds in the spiral arms.
Adapted from <https://www.astro.princeton.edu/eco/research/spurs/project.html>

gas rich discs, spirals could also be a subsequent manifestation of gravitational instability in gas. In this picture, gas could still carry on shocks especially when it has cooled. However, its subsequent structure spurs seem less likely to occur though larger branches are still possible.

Tidal interactions depict a scenario where spirals are induced within the galaxy due to a companion object fly by. Instead of displaying a constant spiral pattern speed, those formed spirals take on a radially dependent pattern speed. In inner disc, spirals behave like arms predicted by density wave theory, however, its pattern speed drops to below the disc rotation speed in outer region⁴.

Triaxial dark matter halo is also considered as a candidate for inducing galactic spirals which is least investigated⁴. Previous studies show that grand two-armed spirals could be formed in gaseous

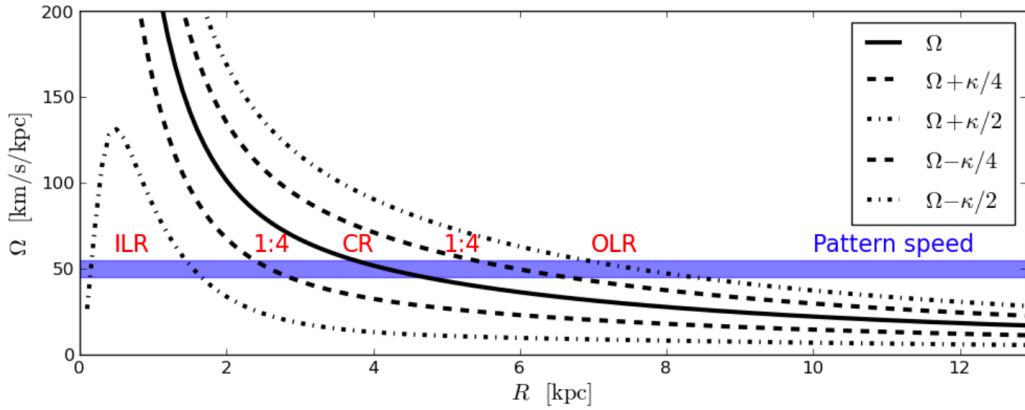


Figure 1.7: Milky Way Galaxy.

Adapted from A.R. Pettitt PhD thesis (2014) Figure 1.10.

discs, on which we would discuss in more details particularly in the following section.

1.3 MOTIVATION

1.3.1 PREVIOUS STUDIES ON DARK MATTER HALO MECHANISM

The flat rotation curve indicates the existence of massive dark matter around the galaxy in order to support the high rotational speed in outer disc. Previous studies show that, in low mass and low surface density gasous disc, extended, persisting two open trailing arms could be developed under a triaxial dark matter halo and those arms would quickly wind up to rings¹⁰. However, the shortcoming of this finding is that the triaxiality of halo is turned on abrupt without a switch-on function and the rotation curve of their galaxy with an even surface density is steep instead of a flat one with an extremely low resolution. Researchers later implemented a linear growth function for Dark Matter Halo triaxiality and various surface density distributions and rotation curves for discs, they found global, long-lived spirals would be certainly induced and they also pointed out that its geom-

etry is highly dependent on parameters of disc such as rotation curve and halo, particularly leading arms always transit to trailing ones at the disc periphery¹¹. Nevertheless, some researchers argue that the appearing spiral structures in the simulation of Khoperskov originate from their non-adiabatic enough introduction of the triaxiality of halos and they also suggest that with a fully adiabatic growth function for halo, spiral patterns are not necessarily formed¹², this could also explain why many rings appear in the outer discs in Khoperskov's simulation because of the abrupt increase of halo triaxiality. However, Hu mainly investigates the response of stellar disc to the halo rather than gas disc. While some other simulations also find the spiral arms induced by triaxial halos and they are the most long-lasting and had the highest-density contrast compared to other mechanisms. Furthermore, they also notice a galactic bar-like structure at the central disk¹³. However, they did not mention halo characteristics and they mainly focus on density distribution of gas response rather than its dynamics. Therefore, whether triaxial Dark Matter Halo could induce spirals in galaxies, peculiarly in MW like galaxies, and how gas responds to triaxial halo perturbation still remains as a puzzle.

1.3.2 THESIS AIM AND STRUCTURE

Though various spiral structures and its formation mechanisms have been investigated since long before, but hardly gas dynamics had been compared between different candidate theories and particularly, spirals induced by triaxial dark halos is least learned. In this thesis, we mainly did two studies. First is how gas disc responds to a adiabatically grown triaxiality of dark matter halo. Second is to compare the dynamic responses of gas to different galactic spiral perturbations in a MW like galaxy.

2

METHODS

2.1 CODE

We use simulation code *Phantom*, a three-dimensional smoothed particle hydrodynamics code^{14 15}.

The advantage of using SPH over a grid-based code is that, since the grid-based method calculates the density based on mesh scheme, which could lead to great errors when sparse and dense areas show up because the calculation of the density of neighboring unit meshes doesn't connect with

each other. This could lead the map of the density not to match the real distribution of mass unless the grid reaches some accuracy. Also, the smoothed particle method has excellent conservation property since energy, liner momentum, angular momentum, mass and entropy are all conserved at the same time. SPH can also be combined with accurate treatments of self-gravity. What's more, some additional treatment of unresolved physical process can also be added at the particle level in SPH such as star formation in galaxy-scale simulation.

Kernel is the key concept in SPH code, which is an interpolating function, we could effectively use discretized points to represent the fluid, but the kernel allows to interpolate the fluid at any arbitrary location by performing a weighted average over nearby particles. It is introduced to avoid inaccuracy when we deal with some certain dense or sparse case like grid-based method does by adjusting the radius R_q (eg. Dense area, a smaller R_a). Since the further a neighbor particle is away from the target, the smaller impacts it exerts on the nearby mass density of the target, when there are point mass particles right on the sphere, a place where is the most far from the target particle within its neighborhood, it could lead to errors if we treat every neighbor particle equally. Kernel is basically a weight function like a probability density function, through which achieves that the contribution of a neighbor particle to local density decreases with its relative distance from the target particle. The parameter to describe the process of falloff is h . And the former equation is then, written as follows:

$$\rho(\mathbf{r}_a) = \sum_{b=1}^{N_n} m_b W(\mathbf{r}_a - \mathbf{r}_b, h(\mathbf{r}_a)) \quad (2.1)$$

Where relative distance and h , the smoothing length, affect on the weight function W . The density at the location of a particle \mathbf{r}_a can then be interpolated from a weighted sum ober neighbouring particles, N_n , at some distances r_b , with mass m_b via using a kernel function W that decays with radius.

2.2 GALACTIC COMPONENTS

This section introduces models of galactic components used in simulations and how we set up the initial surface density following exponential distribution.

2.2.1 INITIAL SURFACE DENSITY

For observed galaxies, surface density of particles on the disc is not uniform, instead, it approximates an exponential distribute as follows:

$$\Sigma(r) = \exp(-r/s) \quad (2.2)$$

The distance of each particle to the central disc is r and how steep the exponential column density curve declines along the radius outwards is controlled by a characteristic scale length, s . Within the maximum radius in our simulations, to generate initial column density in accordance with the above grouping model, we utilize an approach named inverse transform sampling.

From the equation 2.2 , radii cumulative density function (CDF) is primarily acquired after which we could consequently obtain the absorbed normalizing constant as well as the probability density function (PDF). The next crucial step is to build up the inverse function of CDF and plug in a sample of pseudorandom numbers within interval $[0, 1]^*$ in it so as to produce random radii observing equation 2.2 .

Integral of equation 2.2 with regard to r represents the total mass enclosed within radius r and it is shown as:

$$\int_0^{r'} \pi \cdot r \cdot \exp(-r/s) dr \quad (2.3)$$

*In this thesis, pseudorandom numbers are generated by *random* package in Python.

In other words, integrating 2.3 from zero to disc radius with integration by parts, R_m sums up to the disc mass M_d which is also the normalized constant of the CDF.

$$\begin{aligned}
 M_d &= \int_0^{R_m} \pi \cdot r \cdot \exp(-r/s) dr \\
 &= \pi \cdot s \cdot \{s - (R_m + s) \cdot \exp(-R_m/s)\}
 \end{aligned} \tag{2.4}$$

Furthermore, the integrand divided by M_d is subsequently the associated PDF, which not surprisingly only involves with R_m , the maximum radius, and the scale length s . With this approach, we

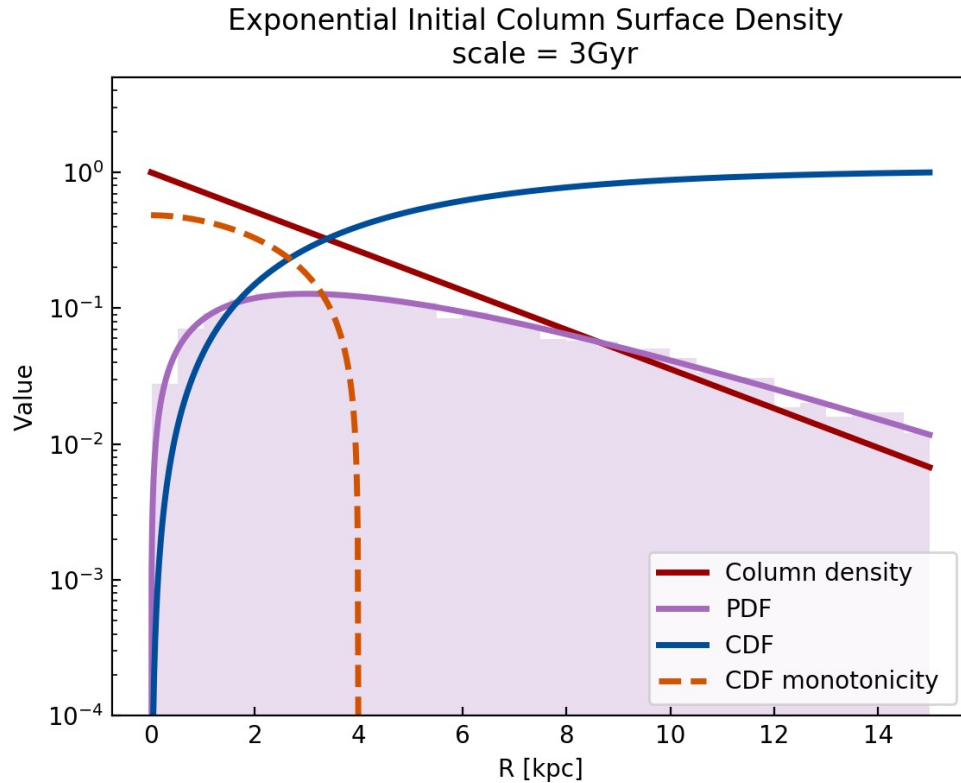


Figure 2.1: This figure presents the probability density function (PDF), cumulative density function (CDF) and surface density for disc at initial setup. The scale length of the disc is 3Gyr.

could circumvent surface density, a two-dimensional physical quantity, and secure the CDF directly as shown below.

$$\begin{aligned} P(r \leq r') &= \frac{\int_0^{r'} \pi \cdot r \cdot \exp(-r/s) dr}{M_d} \\ &= \frac{\pi \cdot s \cdot \{s - (r' + s) \cdot \exp(-r'/s)\}}{M_d} \end{aligned} \quad (2.5)$$

The physics meaning behind the above CDF is the probability of randomly selecting a gas particle whose distance to the central disc is no bigger than r . Consequently, the inverse function of the CDF reflects given a decimal number between zero and one, it returns a value of distance to the central disc. Otherwise speaking, we could secure a group of radii that follows the PDF in equation 2.6 if provided with sufficient number of uniformed pseudorandom numbers within interval $[0, 1]$

$$P(r') = \frac{\pi \cdot r' \cdot \exp(-r'/s)}{M_d} \quad (2.6)$$

Unfortunately, CDF in equation 2.5 is apparently an implicit function which indicates the hardness of attaining its inverse function explicitly. So we begins with shifting all terms in equation 2.5 to one side and rewriting it as a new function shown as below:

$$f(p_i) = (r + s) \cdot \exp(-r/s) + \frac{p_i \cdot M_d}{\pi \cdot s} - s \quad (2.7)$$

The aim is to search for the root of $f(p_i) = 0$ when given a pseudorandom number p_i within interval $[0, 1]$. Notice the CDF is monotonic with $f(0) \cdot f(R_m) \leq 0$, therefore we utilize a root-finding approach called bisection method.

In our context, establish a loop that initially starts with the interval $[0, R_m]$ and find its midpoint r_0 . Then, unless $f(r_0) = 0$ reset the interval as $[r_0, R_m]$ and $[0, r_0]$ respectively by referring the sign

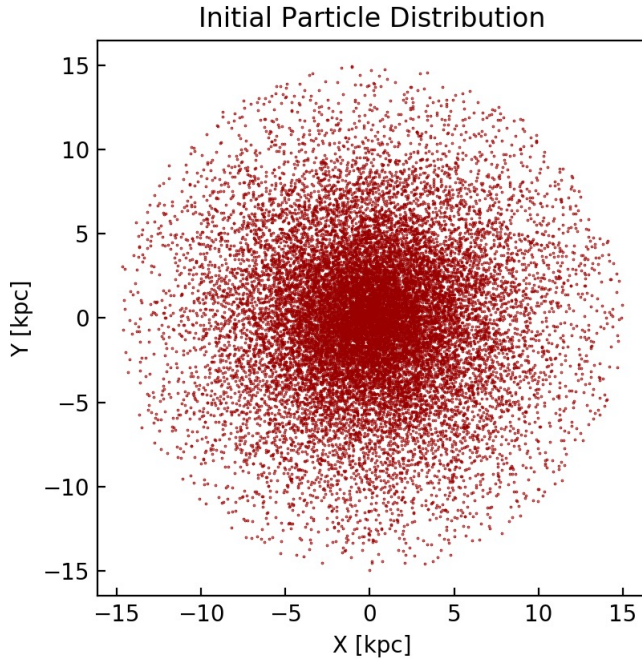


Figure 2.2: An example of 10^5 gas particles being distributed on the disc initially.

of $f(r_0) \cdot f(R_m)$ is positive and negative. This loop terminates until the span of interval is less than a self-assigned precision denoted as ε^\dagger and return the value of r_0 as the root for equation 2.7. Repeat a sufficiently large number ‡ of the process of bisection root-finding for each generated pseudorandom numbers within interval $[0, 1]$, finally the desired distances to the central disc following the equation 2.2 is achieved.

However, this is not the end yet since our simulation codes, *PHANTOM*, reads particle positions based on cartesian coordinates instead of polar coordinates. To resolve this problem, first produce pseudorandom numbers within interval $[0, 2\pi]$, then convert coordinate system according to $x = r \cdot \cos \theta$ and $y = r \cdot \sin \theta$. For the direction z , we simply uniformly distribute gas particles along

[†]All simulations in this thesis set $\varepsilon = 10^{-5}$.

[‡]Numerical tests in this thesis suggest a particle number of more than 10^3 could guarantee a convincing result.

between -1kpc and 1kpc .

Ultimately, we obtain the Cartesian coordinates of each particle and also guarantees them to follow the desired surface density distribution.

see Fig. 2.4. A quick drop-down of the surface density could be found in the outer disc area.

Displays smooth transition at the edge of the disc.

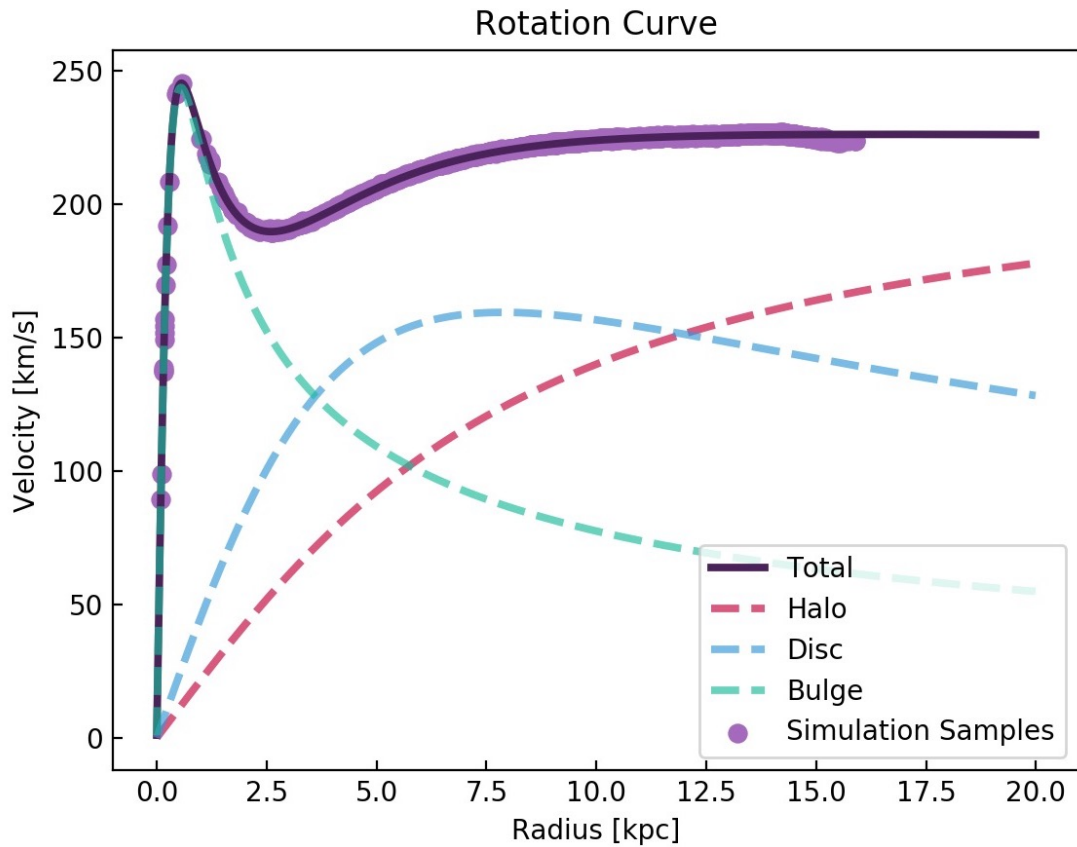


Figure 2.3: Rotation curve of the simulated disc with some simulated gas velocities samples extracted from the initial setup simulation.

2.2.2 MODELS

We used a MW like galaxy which displays a flat rotation curve with a velocity of 220km/s beyond 8kpc. The stellar disc component is the standard Miyamoto Nagai model¹⁶ built in PHANTOM and we choose a Plummer potential in PHANTOM for bulge. Though many literature use Navarro–Frenk–White density profile for dark matter halo¹⁰ but here we adapts and coded the isothermal model¹¹ developed by Koperskov since it reaches a lower limit for DMH to exert impacts on the disc, in other words, if this isotherm halo model could produce arm structures on disc, so does any other halo model.

Figure 2.3 gives the rotation curve of our disc model and the generated samples under those potentials. We run the disc without any perturbations for 2.34Gyr such that the it can reach a better equilibrium state to avoid any potentially artificial ring effects. Figure 2.4 shows better equilibrium state after running without any perturbation brings a less precipitous curve compared with the initial surface density curve and also more smooth transitions both in the central and peripheral disc. To avoid high memory and time consumption, a torus shape gaseous disc with an inner radius of 1kpc and this is used for all simulations that have a resolution of 10^7 particles.

2.3 PERTURBATION MODELS

This section mainly introduce all the perturbation potential models adapted to induce spirals in this thesis. They are quasi-stationary arms, dynamic arms, tidal interactions and triaxial dark matter halo.

2.3.1 QUASI-STATIONARY ARMS

The model we choose for rigidly rotating spirals is developed by Cox & Comez¹⁷ but instead of treating is as a three dimensional analytical potential, here we consider the potential is uniform in

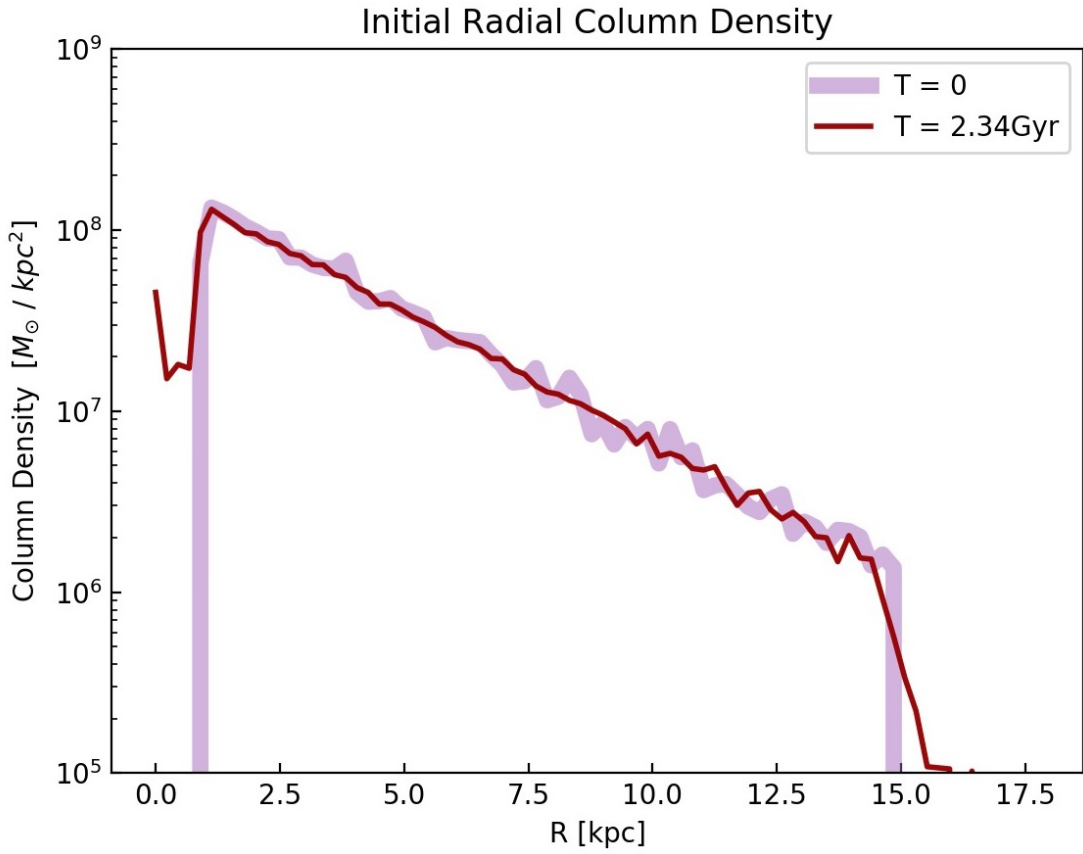


Figure 2.4: This shows initial surface density distribution curve for a disc with 10^7 particles and has a mass of $10^{10} M_\odot$. The dashed curve is surface density at $T = 0$ Gyr and the solid curve shows running the initial disc without perturbations for 2.43Gyr so as to obtain a more equilibrium setup.

the z direction and set the reference angle as zero such that

$$\Phi(R, \phi) = -4\pi GH\rho_0 \cdot \exp((r_0 - R)/R_s) \times \sum \frac{C_n}{K_n D_n} \cos n\gamma \quad (2.8)$$

where

$$k_n = \frac{nN}{R \sin \theta_{sp}} \quad (2.9)$$

$$B_n = K_n H (1 + 0.4 K_n H) \quad (2.10)$$

$$D_n = \frac{1 + K_n H + 0.3(K_n H)^2}{1 + 0.3K_n H} \quad (2.11)$$

$$\gamma = N[\varphi - \frac{\ln(R/r_0)}{\tan \theta_{sp}}] \quad (2.12)$$

where all the involved key parameters are noted as below,

N :	number of spiral arms
θ_{sp} :	pitch angle
ρ_0 :	density at r_0
R_s :	radial scale length of the arm
H :	scale height of the arm
C_n :	profile of the sinusoidal potential

To avoid possible complicated substructures along the main spirals, we set the $C_n = [1, 0, 0]$ since it creates a classical sinusoidal pattern in the density instead of $[8/3\pi, 1/2, 8/15\pi]$ suggested in the original potential, which gives an interarm profile and seems to promote the growth of additional branch features¹⁸. This potential allows us to control the key characteristics of the developed arms such as its pitch angle, pattern speed and arm number. Here we choose a pattern speed of 10km/s/kpc to avoid substructures. The co-rotation term is added in terms of the rotation curve as below¹⁸,

$$\varphi \Rightarrow \varphi + \frac{V_p(R)}{R} \times (t - t_0) + a_p \quad (2.13)$$

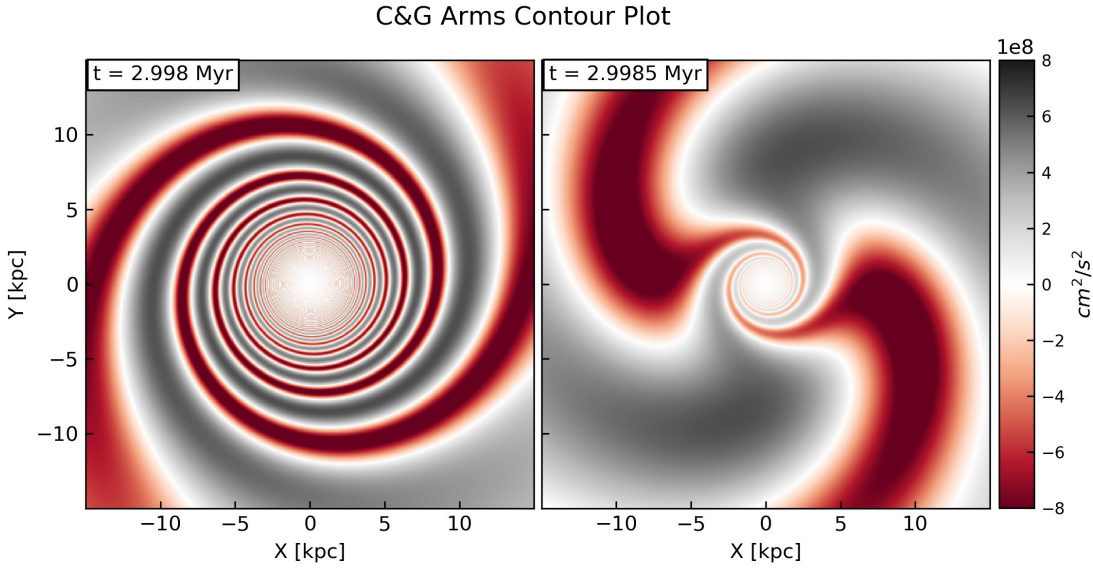


Figure 2.5: Contour plot of dynamic arm potential before t_0 . Note the rotation direction of the simulated galaxy is clock-wisely.

2.3.2 DYNAMIC ARMS

The implementation of dynamic spiral arm potential is developed by Hunt¹⁸, which make the original quasi-stationary spirals into a co-rotating, winding arms and initially designed to solve the swing amplification for stellar disc.

where $V_p(R)$ is the circular velocity and t_0 is the time when potential changes pointing direction from clockwise to counter-clockwise, which marks the strongest spiral strength. In our simulations, we set t_0 as 29Myr and initial position angle α_p as zero. To control the strength of the arms so as to mimic the decrease in spiral amplitudes as spirals evolve,

$$A(t) = \exp\left(-\frac{[t - t_0]^2}{2\sigma^2}\right) \quad (2.14)$$

where σ is the standard deviation of the Gaussian that determines spiral lifetime. Here in our simula-

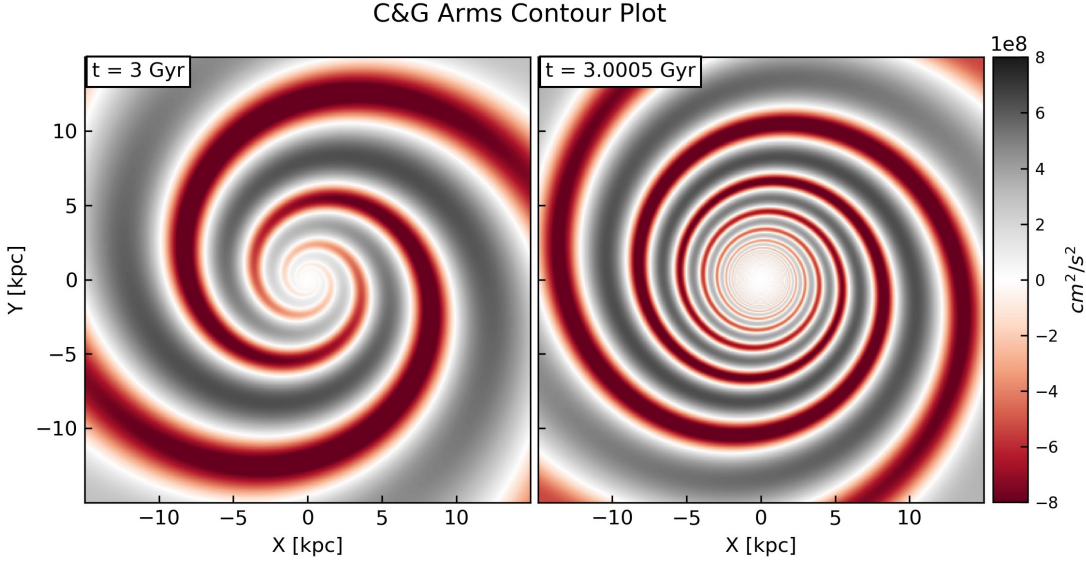


Figure 2.6: Contour plot of dynamic arm potential after t_0 . Note the rotation direction of the simulated galaxy is clock-wisely.

tions, we set it equal to 43 Myr such that could contribute to the most long-lasting spirals induced by this dynamic potential suggested in Hunt et al¹⁸.

2.3.3 DARK MATTER HALO

The model of dark matter halo in which the gaseous disc embeds is treated as an analytical potential.

Though, several models for halo density ρ_h have been introduced in previous studies but in all cosmological either simulations or observations, all indicate haloes are roughly ellipsoidal. Ellipsoidal are characterized by its major axis a_x , middle axis a_y and minor axis a_z . Oblate ellipsoids describes the shape when $a_x \cong a_y < a_z$ which resemble pancakes. Prolate ellipsoids depicts sausage-like shape where $a_x > a_y > a_z$ while triaxial ellipsoids are in between prolate and oblate. According to the latest observation based newly released GAIA data¹⁹, The Milky Way galaxies are inclined to be prolate and axis ratio approximately equals to $q = 0 \sim 0.1$.

In the light of the above, here, we implement the triaxial model in khoperskov's paper.

$$\Psi_b(x, y, z) = 4\pi\rho_{b0}a_x \cdot \left(\ln \xi + \frac{\arctan \xi}{\xi} + \frac{1}{2} \ln \frac{1+\xi^2}{\xi^2} \right) \quad (2.15)$$

G is the gravitational constant. ρ_{b0} is the central density profile of halo,

$$\rho_{b0} = \frac{M_b}{4\pi a_x^3 [R/a_x - \arctan(R/a_x)]} \quad (2.16)$$

ψ is constructed by the three characteristic axes and after plugging the semi-axis ratio relation, the equation (1.3) could be simplified so that the equation (1.1) which describes the triaxial halo now turns into a function with two free parameter q and a_x only.

$$\xi = \sqrt{\frac{x^2}{a_x^2} + \frac{y^2}{a_y^2} + \frac{z^2}{a_z^2}} = \sqrt{\frac{y^2 + q^2(x^2 + z^2)}{a^2 q^2}} \quad (2.17)$$

The force of each particle under this analytical potential along x,y are represented as below respectively. The halo should grow from a spherical one into the triaxial shape gradually so as to ensure the way of introducing the halo won't be the trigger of spirals. In previous studies, triaxial halo were introduced either linearly or all of a sudden and in Hu's paper, which deals with stellar discs, points out that triaxial halos are not necessarily to be the source of inducing spirals as long as the halo grows in a fully adiabatic way. Therefore, to clarify, we work on three different switch-on functions for the development of halo for the gaseous disc which are linear, polynomial and modified exponential.

In our simulations, the triaxiality of halo is fully turned on through 1Gyr and 3Gyr in order to compare the characteristics of induced spirals in react to the influence of time-scale. We implemented three growth functions used by different literature for halo growth to test if to which the development of spirals is sensitive.

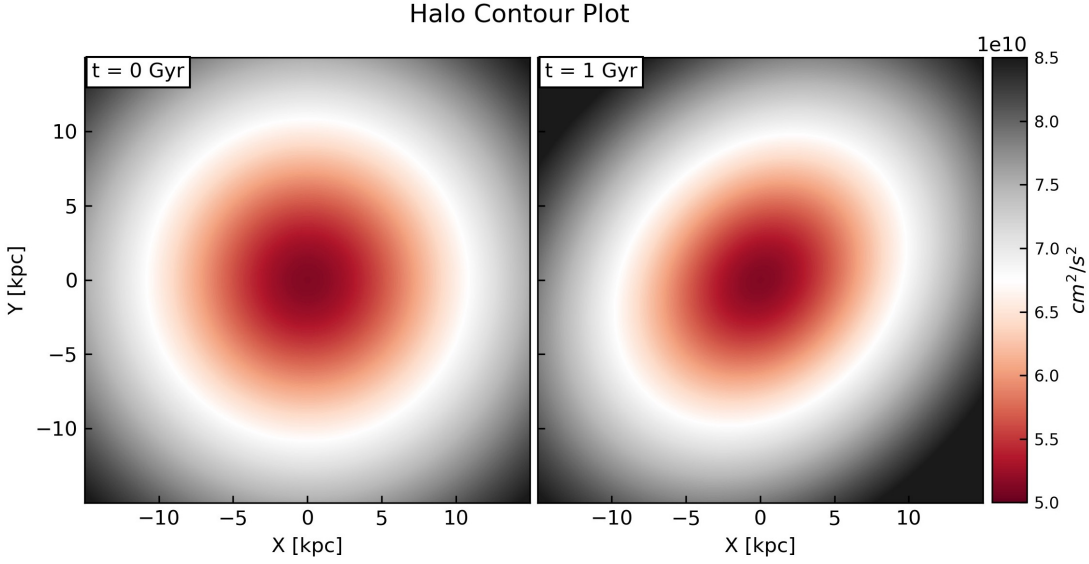


Figure 2.7: Potential contour plot of triaxial halo. Note in our simulations, halo is set to be static.

The first one is a linear growth, which is tested by Koperskov ¹¹. With this function, triaxiality of halo is fully switched on linearly from $q = 0$ to $q = 0.1$ within in 1Gyr. The second one is developed by Dehnen ²⁰, we follow the function which is suggested to grow bar in our simulation to let halo evolve gradually.

$$A_b = q \cdot \left(\frac{3}{16} \xi^5 - \frac{5}{8} \xi^3 + \frac{15}{16} \xi + \frac{1}{2} \right) \quad (2.18)$$

where q is the halo triaxiality, and ξ is,

$$\xi = 2 \frac{t}{t_1} - 1 \quad (2.19)$$

where t_1 is the time taken by halo to fully turned to $q = 0.1$.

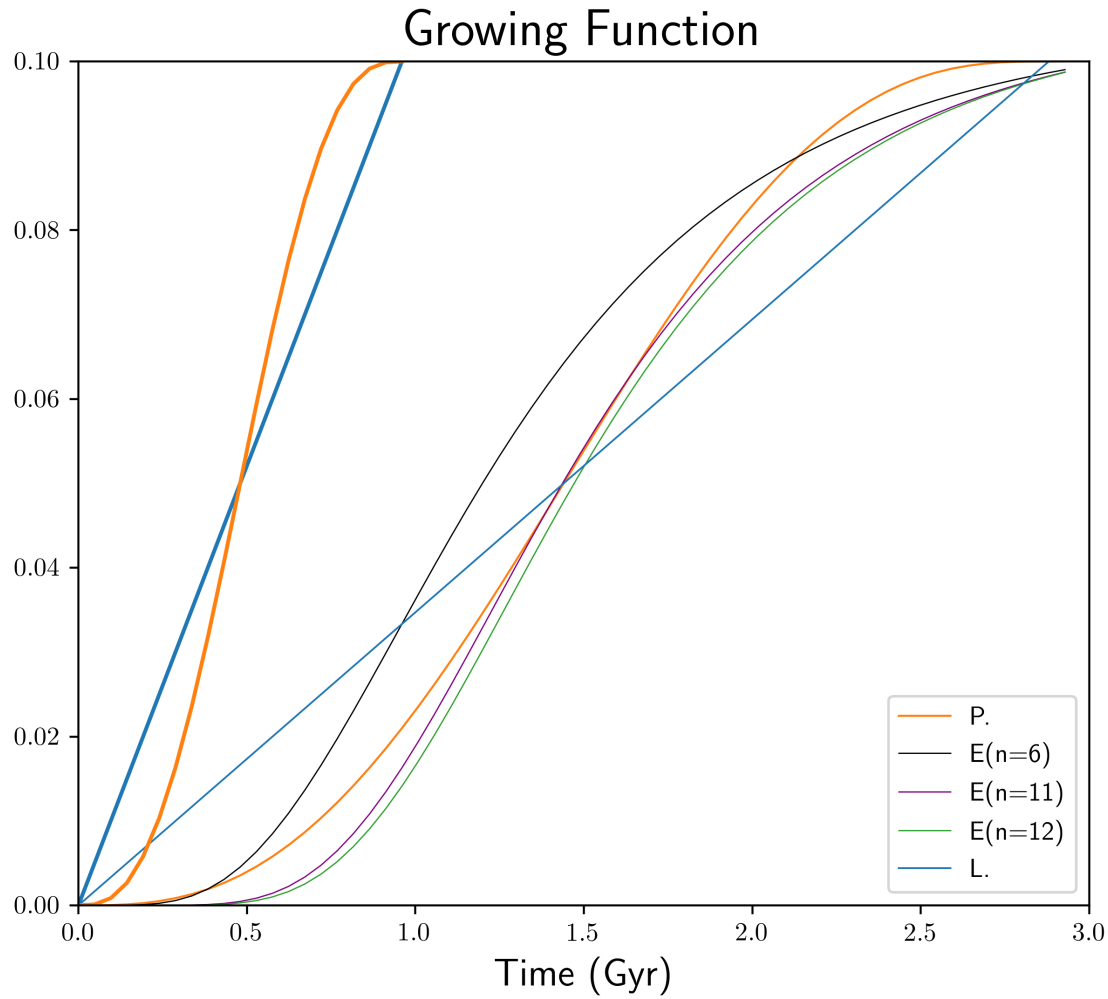


Figure 2.8: Activation functions for triaxiality of halos are divided into three categories, linear(L), polynomial(P) and exponential(E).

The third growth function follows an exponential form which is developed by Hu et al¹²,

$$f(t) = 1 - \exp(-t/\tau_1) \quad (2.20)$$

$$f_n(t) = \left\{ 1 - \frac{1}{n} \exp^{-\frac{t}{\tau_1}} [1 + (n-1) \exp^{-\frac{t}{\tau_1}}] \right\}^n \quad (2.21)$$

2.3.4 TIDAL COMPANION

The adapted potential for tidal interaction is developed by Sellwood²¹, which observes the idea from Toomre²² that the internal tidal forces within each component approximates as a rotating quadruple perturbation and reaches the strength summit only during the period of peri-center passage.

We convert the potential from its original spherical representation to cartesian coordinates and absorb the rotation term in axis rotation in simulation such that,

$$\Phi_t(x, y) = A_m \Phi(x, y) e^{(t-t_0)^2/2\tau_i^2} \quad (2.22)$$

$$A_m = -\frac{GM_b \alpha_2}{a_1^3} \quad (2.23)$$

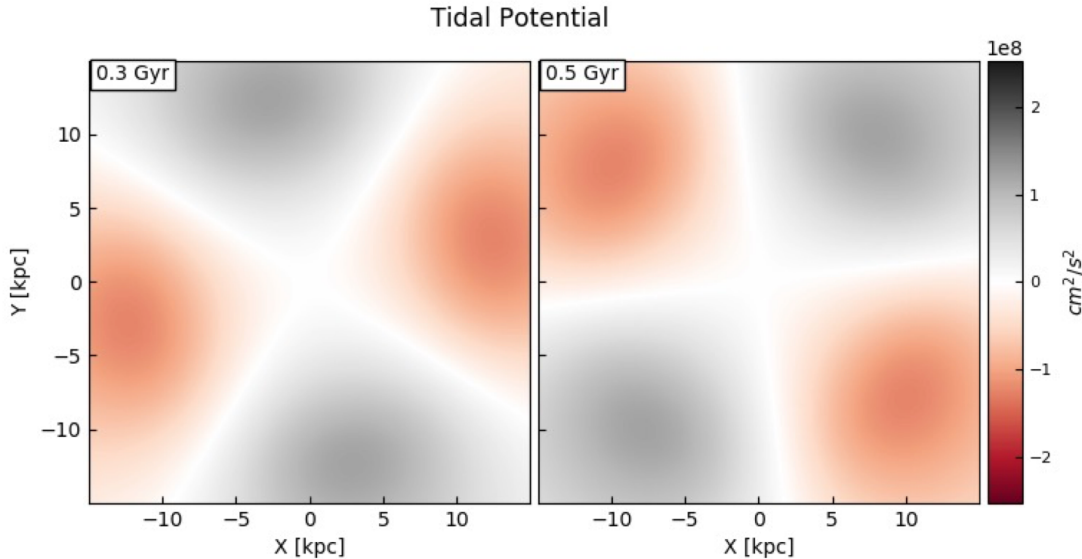


Figure 2.9: Potential contour plot of tidal interaction.

$$\Phi(x, y) = (x^2 + y^2) \cos(2 \arctan \frac{x}{y}) / \{1 + \frac{(x^2 + y^2 + z^2)^{5/2}}{\alpha_1^2 \beta_2^2}\} \quad (2.24)$$

where τ_t is the approximate duration of the peri passage and be set up equal to pattern speed of the potential $1/\Omega_p$ and let $t_0 = 2.5\tau_t$ such that the peri-approach happens around 0.42Gyr. A_m is the constant term. α_1 represents the semimajor axis of the bar and equals to 20kpc. We also set the other two semimajors as $\alpha_2 = \alpha_3 = \frac{1}{2}\alpha_1$. M_b is the mass of the companion and equals to 3.6×10^9 such that the summit perturbation at the edge of the disc is 2.5% of the centripetal acceleration at the same location. Potential pattern speed Ω_p is settled as V_c/α_1 with V_c equals to 220km/s. α_2 and β_2 , which equal to 0.7190 and 0.6901 respectively²³, are dimensionless constants that corresponds to the axis ratios $\alpha_1 : \alpha_2$ and $\alpha_1 : \alpha_3$.

3

Results

Here we present results of our simulations into different spiral generation mechanisms on the interstellar stellar medium.

3.1 ANALYSIS TECHNIQUES

3.1.1 GAS DYNAMICS

Firstly, we divided the disc into rings such as when provided a particle position, we could calculate its radius and in which ring it drops in through the following equations,

$$\begin{aligned} r_i &= \sqrt{(x_i^2 + y_i^2)} \\ \frac{r_i}{R_M} &= \frac{n_{ri}}{n_R} \Rightarrow n_{ri} = \frac{r_i \cdot n_R}{R_M} \end{aligned} \quad (3.1)$$

where r_i is the gas distance to the disc center, R_M is the disc radius, in our simulation, this value as 18kpc and n_{ri} is the index of ring that the particle locates in which is rounded to an integer. n_R is the total number of rings the disc is split into, which is 80 in our simulation.

Secondly, we further cut the ringed disc into slices. The disc is divided into four quadrants and each quadrants is sliced into 100 pieces represented by n_Θ . The radial and azimuthal velocities can be calculated after knowing which quadrant it falls in as follows,

$$\begin{aligned} v_r &= v_x \cos \theta + v_y \sin \theta \\ v_\theta &= v_y \cos \theta - v_x \sin \theta \end{aligned} \quad (3.2)$$

the index of slice in which a gas particle drops is determined by the following equations,

$$\begin{aligned} n_{1\theta i} &= 2n_\Theta \cdot \arcsin(y_i/r_i)/\pi \\ n_{2\theta i} &= 2n_\Theta \cdot \arccos(x_i/r_i)/\pi + n_\Theta \\ n_{3\theta i} &= 2n_\Theta \cdot \arcsin(y_i/r_i)/\pi + 2n_\Theta \\ n_{4\theta i} &= 2n_\Theta \cdot \arccos(x_i/r_i)/\pi + 3n_\Theta \end{aligned} \quad (3.3)$$

where $n_{1\theta i}$ calculates the index of piece for particles in the first quadrant and $n_{2\theta i}, n_{3\theta i}, n_{4\theta i}$ does the

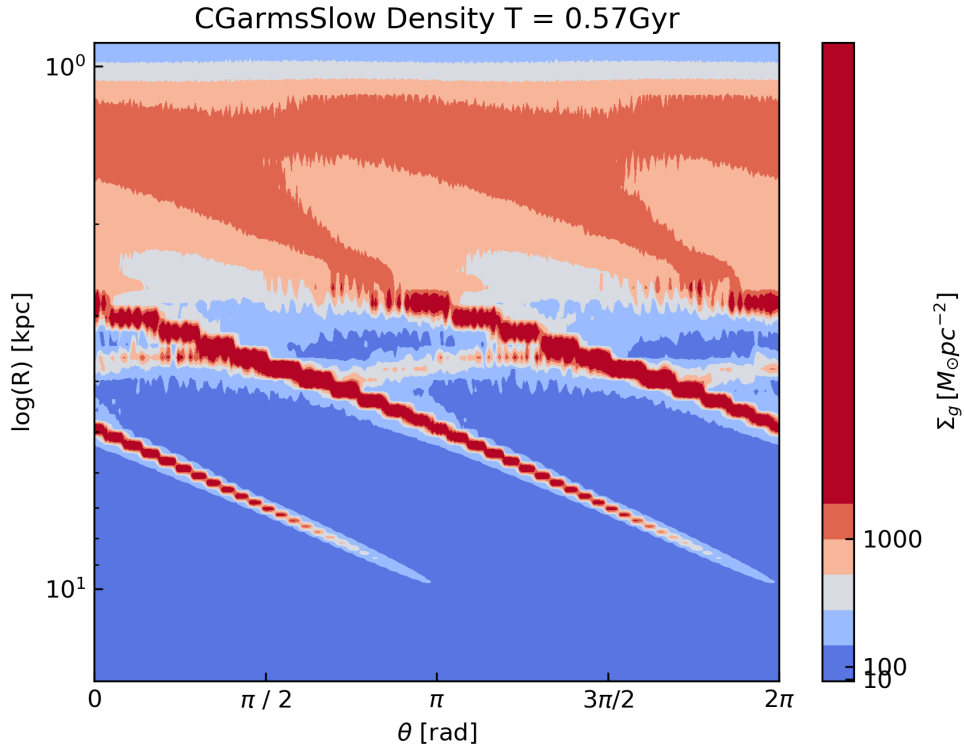


Figure 3.1: This heatmap enables us to check whether the induced arms are logarithmic or not.

same work for second, third and fourth quadrant respectively.

The obtained indexes of ring and piece of each particle is the key to refer the particular particle and then gather particles with same label and get the total number in each grid. Divide the quantity by sector area, we would get the density in this grid as well as radial velocity and azimuthal velocity by summing up those velocities of each particle and then, obtain the heatmap for each physical quantity.

We also give the logged $r - \theta$ heatmap for density, which enables us to check whether the induced arms are logarithmic or not. fig. 3.1 shows logarithmic arms displaying a straight line on the heatmap.

3.1.2 FOURIER ANALYSIS

In order to quantitatively analyze the developed arms, we follow the method Fourier analysis in ²⁴ to decompose the spirals. Taking a slice of data with a fixed radius from the obtained $\theta - r$ map in the last section and performing the Fourier analysis on it, we could reveal the several characteristic quantities about the induced arm.

For each radii, we grid them into sectors in which store density and velocity information of particles in that grid. Take density for example, we calculate the average density for each grid at a certain radius and fit this set of density data with Fourier decomposition shown as below with *scipy.optimize* in *Python*.

$$I(r) = 1 + \sum_{m=1}^{\infty} A_m(r) \cos m[\varphi - \varphi_m(r)] \quad (3.4)$$

where A_m refers to the arm amplitude, m is the mode which also stands for arm number and $\varphi_m(R)$ is the phase angle. To avoid any artificial boundary effects, we only do the fitting for radii ranging from 2kpc to 7kpc. According to our simulation results, we found the dominate mode is always two. Thus, we tick out φ_2 for each radii and adjust them in terms of the signal of their corresponding amplitude A_2 . For instance, if A_2 is positive, we keep the original φ_2 given by *Python*, if it is negative, we increase the phase by $\pi/2$. Furthermore, sometimes the fitting parameter φ_2 could also be both negative and postive. we also need to readjust to guarantee that the phase angle sequence should be following a monotonically increasing pattern to ensure it goes accordance with the shape of an open arm and also keep the phase difference between two adjacent phase angles being less than π . The last but not least thing is to subtract all elements in this phase set by $\varphi_2(r = 2)$ in order to make the phase sequence starts from 0.

After acquiring groups of adjusted phase angles for density, averaged azimuthal velocity and radial velocity, we could plot the $\varphi_2 - r$ diagram so as to investigate and compare the relationship

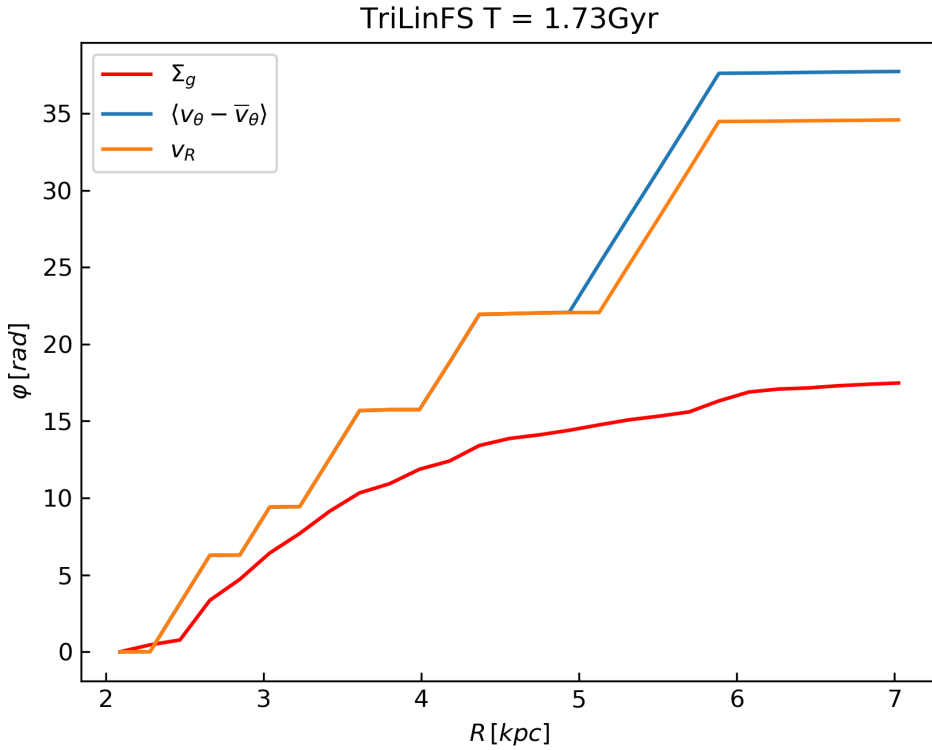


Figure 3.2: Adjusted phase angles for density, averaged azimuthal velocity and radial velocity from 2kpc to 7kpc.

between them which reveals the dynamics of gas in response to each galactic potential. Note that as gas moves in and out of the spiral area, this passage could bring up shocks and other small scale structures such that influences the offsets between phases of density and velocities⁴.

Here we give an example see fig. 3.2 of offset diagram which is taken from the triaxial dark matter halo case.

3.2 DARK MATTER HALO

3.2.1 LOW RESOLUTION

Before we jump into the analysis of triaxial dark matter halo effects on the morphology of gaseous disks, we pre-simulate with a lower resolution of 10^4 particles and the bulge-free disk mass equals to $10^{10} M_\odot$ in an isothermal context where $T = 10^3$ K. To match with the previous studies ¹⁰, we adapt a disc with an uniform surface density distribution for the initial setup. We do observe grand design two-armed structure in our disk in case where no growth function is performed on the halo, which is consistent with those in past studies though we used different dark matter halo models but it makes sense because the isothermal model satisfies the lowest limit of having impacts on the disk. If a polynomial growth with a full activation time of 1Gyr is added on the halo, no arms appear unless an increase in resolution. With a higher resolution, a bar-like structure would come into sight in the central disk, which had been observed in study ¹³. In the inner region of disk, it also shows leading arms with a small amplitude compared with those in outer region. This also matches with the results in ¹¹ stating leading arms always become trailing spirals at the periphery and produce complex Θ -like structures.

Under this condition, two-armed long standing leading arms could be generated with a higher temperature $T = 10^4$ K in isothermal context. Furthermore, the strength of arms could be enhanced when we increase the triaxiality of the halo from $q = 0.1$ to $q = 0.2$. Even though the color contrast shown in the plot indicates the amplitude of arms would be fairly strong, arms could be not formed when we execute an extremely adiabatic growth function on the halo, which could either be the polynomial function with a duration of 3Gyr or the exponential growth with a n above 8.

We found that resolution, temperature and particularly, growth functions play a vital role in inducing arms under dark matter halos.

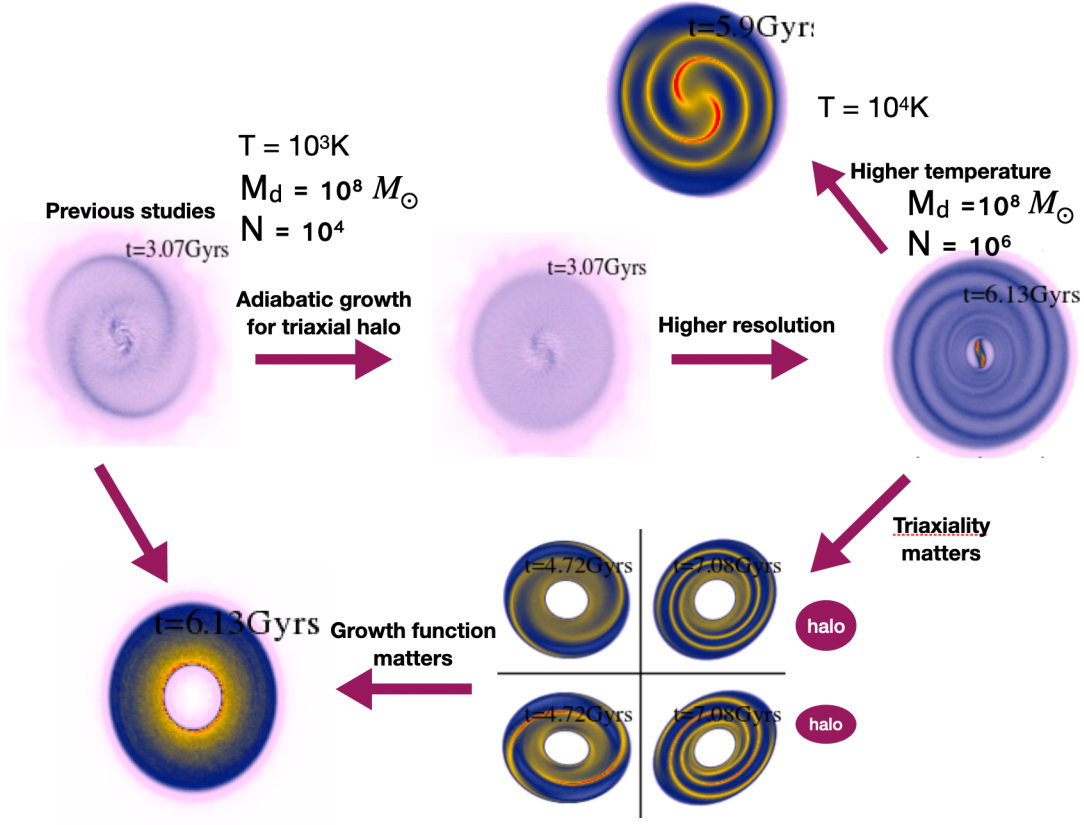


Figure 3.3: Low resolution simulation results of triaxial dark matter halo. This demonstrates resolution, temperature and particularly, growth functions play a vital role in inducing arms under dark matter halos.

3.2.2 HIGHER RESOLUTION

In the preceding subsection, we have discussed triaxial dark matter halo effects on generation of arms and the results shows accordance with previous studies except we indicated that triaxial dark matter halos does not necessarily induce arms within a gaseous disk when its growth function is adiabatic. This result goes in accordance with Hu's study since spirals also do not show up in their stellar galactic disc when they execute a adiabatic triaxial halo.

In this subsection, we run a resolution of 10^7 for isothermal case with a temperature $T = 10^3 \text{ K}$. Instead of using a uniform disk as the initial setup, we adapt a disk with exponential distribution

List of Performed Simulations of Triaxial Halo				
Job ID	Bulge	Triaxiality	Growth function	Switch-on time [Gyr]
TriLinWeakFast	Yes	0.1	Linear	1.0
TriLinStrongFast	Yes	0.2	Linear	1.0
TriLinFS	Yes	0.2	Linear	0.5
NBTriLinSlowWeak	No	0.1	Linear	0.1
NBPolySlowWeak	No	0.1	Polynomial	0.1

Table 3.1: The different calculations performed with triaxial dark matter halos. All the halos we simulated are static with no orbital speed.

and a flat rotation curve with an extended velocity of 220km/s. The list of performed simulations for triaxial dark matter halo is shown in Table 3.1. *TriLin WeakFast* stands for a triaxial halo whose triaxiality is linearly switched on from spherical to $q = 0.1$ within 1Gyr while *TriLinStrongFast* has a maximum of triaxiality of 0.2. *TriLinFS* adapts a polynomial growth with 0.2 as its largest triaxiality.

Further, we plot the logged $r - \theta$ heatmap for *TriLinFS* around $T = 1.7\text{Gyr}$ since the strength of spirals appears to be the strongest. We have found that those spirals are notable and two-armed. Interestingly, they are not typical logarithmic arms since in this logged heatmap, induced spirals does not fallow a straight linear line but curve instead.

For simulation *TriLin WeakFast*, no spiral structure is induced by the halo as shown in 3.4. As we increase the triaxiality of halo in simulation *TriLinStrongFast*, We could see that the extreme weak trailing arms appear in outer region of the gaseous disc and its strength summit is not synchronized with that of triaxiality of halos as those induced spirals become stronger and stronger after 1Gyr which is the switch-on time. Moreover, the disc becomes more squeezed as the halo now has a higher triaxiality, which is as what we conjectured. Though spirals are generated, they are not as intense as we have found in previous low-resolution bulge-free disc cases. we assume it might have been the triaxiality of the halo is not high enough. We then run simulation *TriLinFS* in which the triaxiality of halo grows at a faster speed. As shown in figure 3.4, disc becomes extreme sqeezed at an

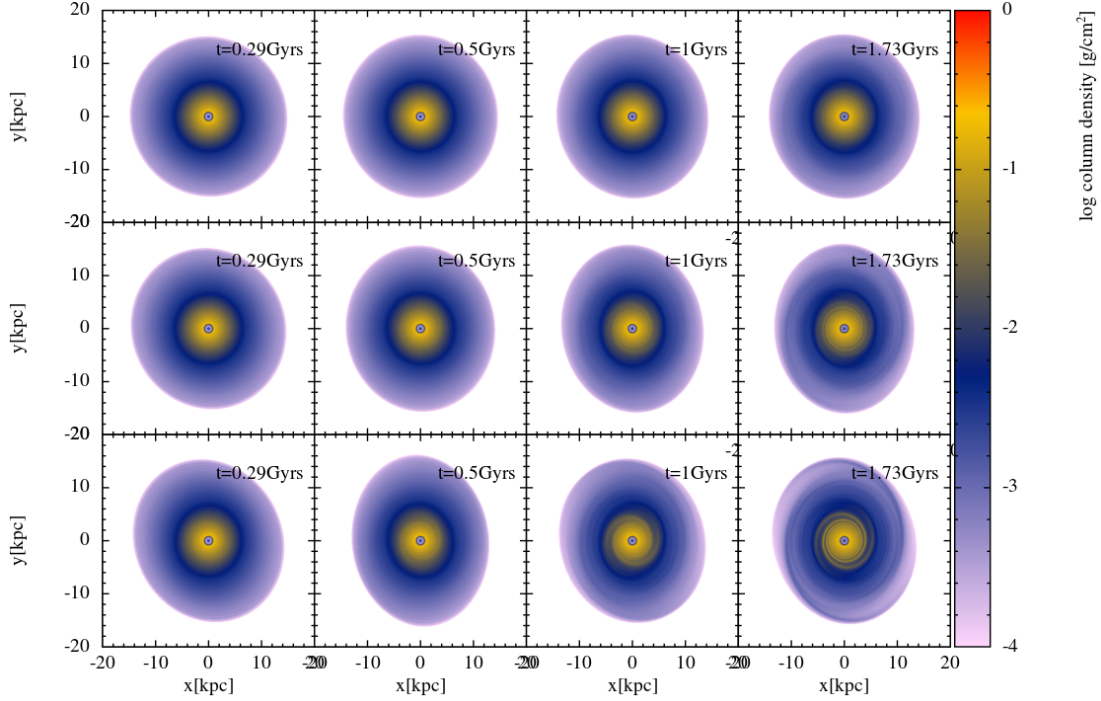


Figure 3.4: This figure shows disc 2D density distribution of triaxial dark matter halo with a flat rotation curve and exponential initial setup. The first panel displays results of *TriLinWeakFast*, the middle panel shows results of *TriLinStrongFast* and the last panel is *TriLinFS*. We could see weak trailing arms only developed given a condition where halo grows at a fast speed and a high triaxiality.

earlier stage compared with the *TriLinStrongFast* and the developed arms show a higher amplitude.

In inner region of the disc, we could also notice more explicit two-armed trailing arms which is not clear in *TriLinStrongFast*. However, a triaxiality of 0.2 is not favoured by the current cosmological simulation for a prolate halo¹⁹. We did not run more simulations with more adiabatic growth since a linear and fast enough halo already shows extreme weak spirals.

The main difference in the parameter profile between our simulations and the previous literature are initial particle distribution and rotation curves, which contributes our motivation to run same level of resolution for bulge-free discs and figure 3.6 displays the results. In *NBTriLinSlowWeak*, with a linear growth, we could observe a bar-like structure is developed in the central disc and on

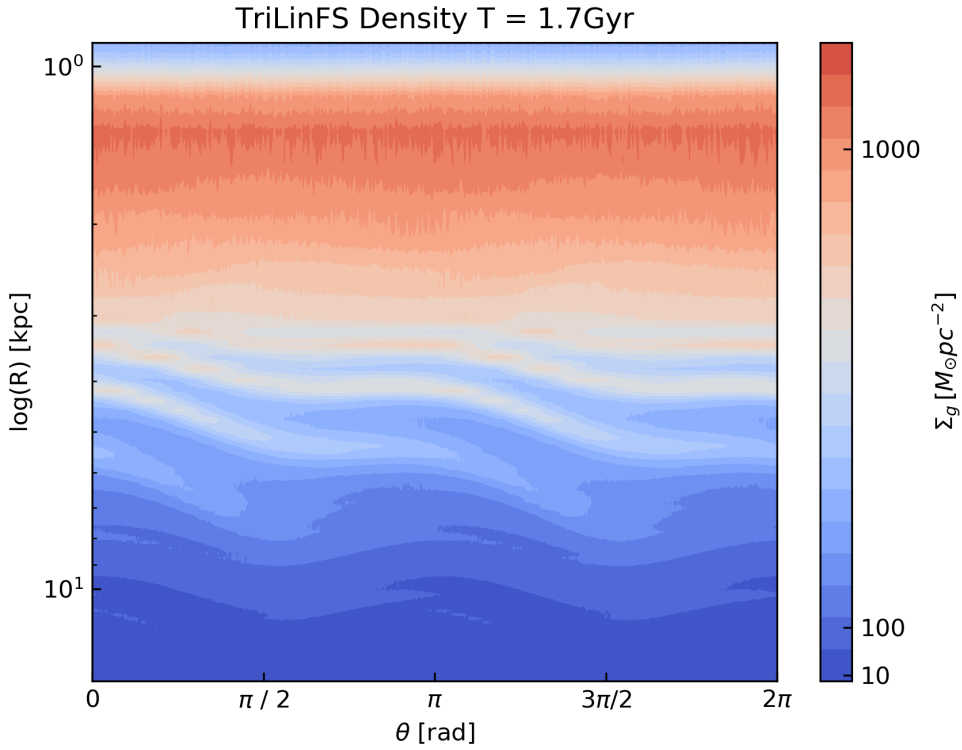


Figure 3.5: This figure shows contour plot logged $r - \theta$ density heatmap of simulation *TriLinFS* at $T = 1.73\text{Gyr}$. It indicates that the triggered arms by triaxial halo are not logarithmic arms.

its two ends, two-armed leading arms with a strong amplitude are induced and transit to weak trailing arms as it extends to outer disc. The pitch angle of those developed arms is very small and the arms are static since the halo does not rotate in our simulations. Our results deviate from the previous studies since no long-standing leading arms were observed in past literature stating leading arms appear and quickly transfer to trailing arms through a Θ stage. We suspect this is due to the initial particle distribution in the disc. Furthermore, we obtain the logged density plot figure 3.5 for *TriLinFS* at time 1.73Gyr since it is the only output showing noticeable spirals. Apparently], the induced arms are not logarithmic or they should display a linear straight line on the heatmap.

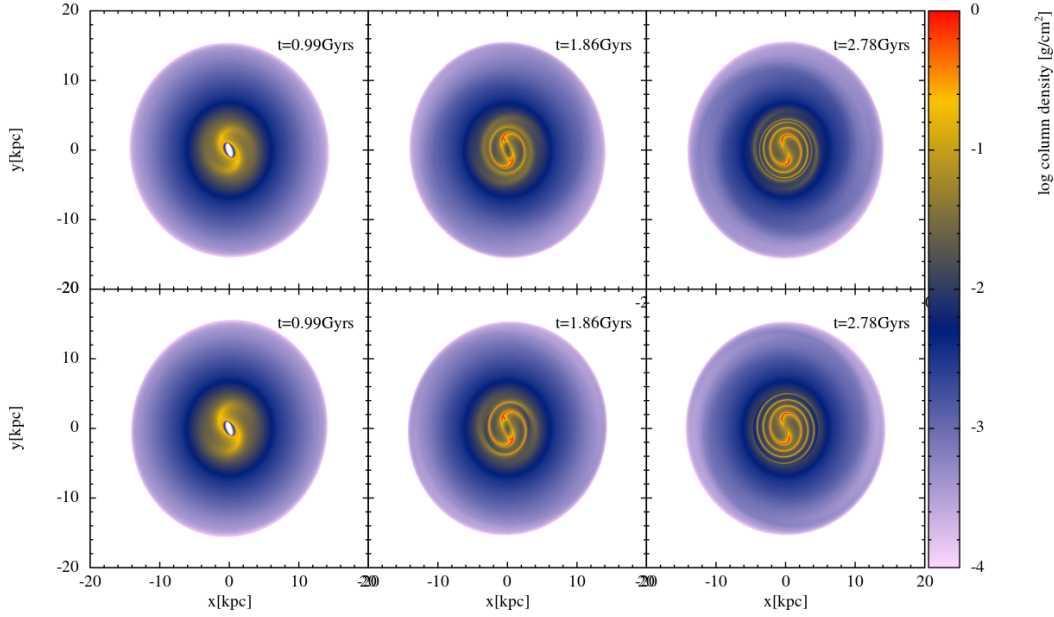


Figure 3.6: This figure shows disc 2D density distribution of bulge-free triaxial dark matter halo with a steep rotation curve and exponential initial setup. Strong leading arms are both developed in inner disc on the ends of a bar-like structure. The induced weak trailing arms extends to the peripheral disc.

The obtained results of gas dynamics for simulation *TriLinWeakFast* is demonstrated by radial and averaged azimuthal velocities as well as the offset plot. Figure 3.7 shows triaxial halo effects on disc brings compression of gas particles in both radial and azimuthal directions suggesting by the red and blue bands in the heatmap. The distribution of these two color bands displays a dislocation. Furthermore, this gas compression becomes more intensive as the triaxiality grows as the color of bands turns darker. After the peak of triaxiality passes, we could tell arms are developed because of the appearance of stripe structure in the red and blue bands, though arms are shown extremely weak in density heatmap.

To investigate the phase relation between the density, azimuthal velocity and radial velocity, we plot the offset diagram for *TriLinStrongFast* and *TriLinFS* around $T = 1.7\text{Gyr}$ at mode $m=2$ since no strong enough spiral structure are induced in *TriLinWeakFast*. From Figure 3.8, we could

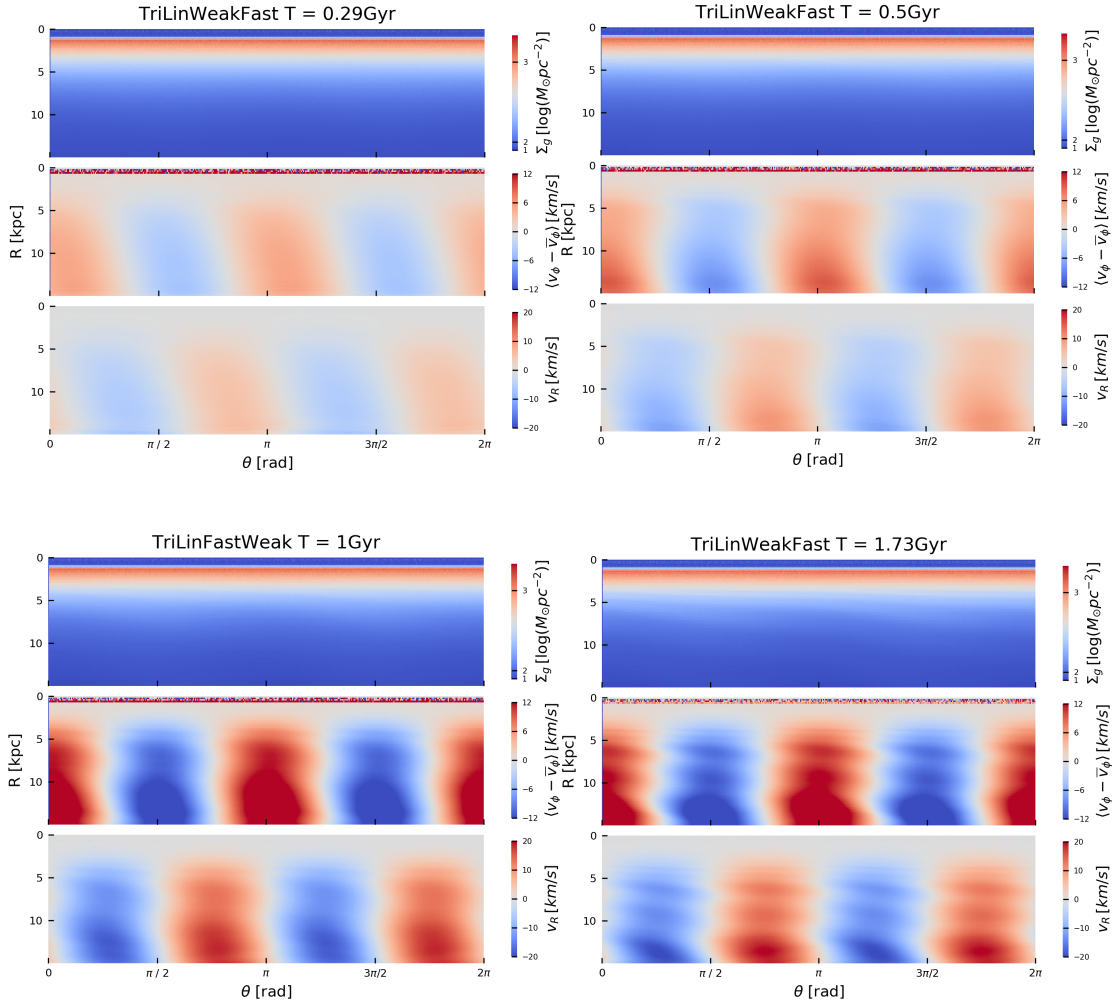


Figure 3.7: These heatmap of density, averaged azimuthal velocity and radial velocity are for simulation *TriLinWeakFast*. Red and blue bands suggest gas compression and it displays stripe structure as the arms show up.

see, overall, all phases of the three physical quantities grow at a relative identical speed and reaches a plateau in the end. Note here we exclude the peripheral disc to drop the boundary effects. The phase curve of averaged azimuthal velocity and radial velocity indicates an offset, which might originates from the dislocation between red and blue bands as we discussed before.

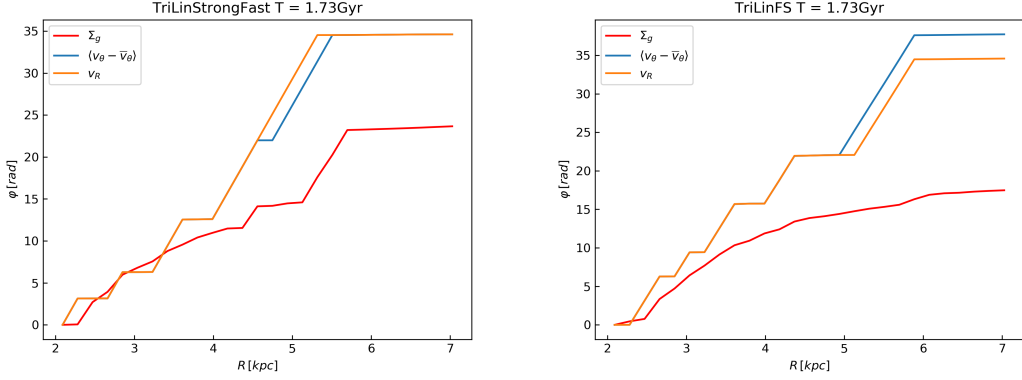


Figure 3.8: This figure shows the phase change and relation between density, azimuthal and radial velocity of gas particles at mode $m=2$ of simulation *TriLinStrongFast* and *TriLinFS* around $T = 1.73\text{Gyr}$ since moderate spirals are developed in the disc. It displays a plateau where all the three phase curves reach and an offset between averaged azimuthal velocity and radial velocity.

3.3 TIDAL INTERACTION

In this section we present the results and analysis we have obtained from tidal interaction. Figure 3.9 shows the density distribution in the disc at $T = 0.5\text{Gyr}$, where the perturbation peaks at, and the following three peri-galacticon time. Two grand trailing arms are developed after the closest approach of the tidal component and the induced arms are long-standing enough to last more than several peri-galacticon time, which is mostly because the galaxy inner environment in our simulation is rather simplified without any dissipation factor to those arms. We could also notice that arms are also tighter in the inner disc than that of the outer disc. Moreover, weak winding effect could also be found as time goes by.

We then plot the logged $r - \theta$ density heatmap to check if these arms are logarithmic. As what the figure 3.10 demonstrates, those extended arms induced by tidal interaction are not logarithmic but they do evolve into a much linear and thinner tightened line after the passage of the tidal component as time persists. Note that the squared structures along those lines are artifacts because of

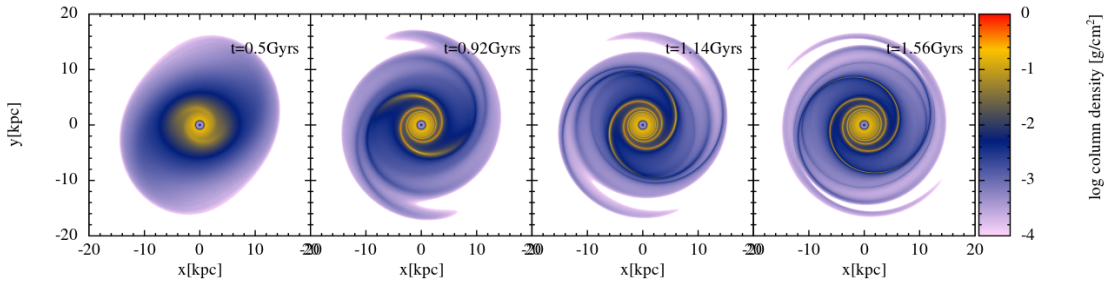


Figure 3.9: This figure shows 2D density distribution for disc encounters a tidal component at time when perturbation peaks and the following three peri-galacticon time. Two extended trailing arms are induced and winding effect is also noticeable.

the low resolution in slicing the disc. If we adapt a higher resolution, those pattern could disappear and are replaced by more smooth curves, but as a compromise, the Fourier fitting process can be extremely time-consuming.

The offset diagram of density, averaged azimuthal velocity and radial velocity shows in figure 3.9, we could see A big gap only shows up between phases of density and velocities at large radius at the peak perturbation. Furthermore, phases change faster as time passes by and all of them show consistent growing speed in phase changes. In other words, there is a time-dependence in the location of the phase density and the velocities, which could in principle be used to infer when the original interaction took place.

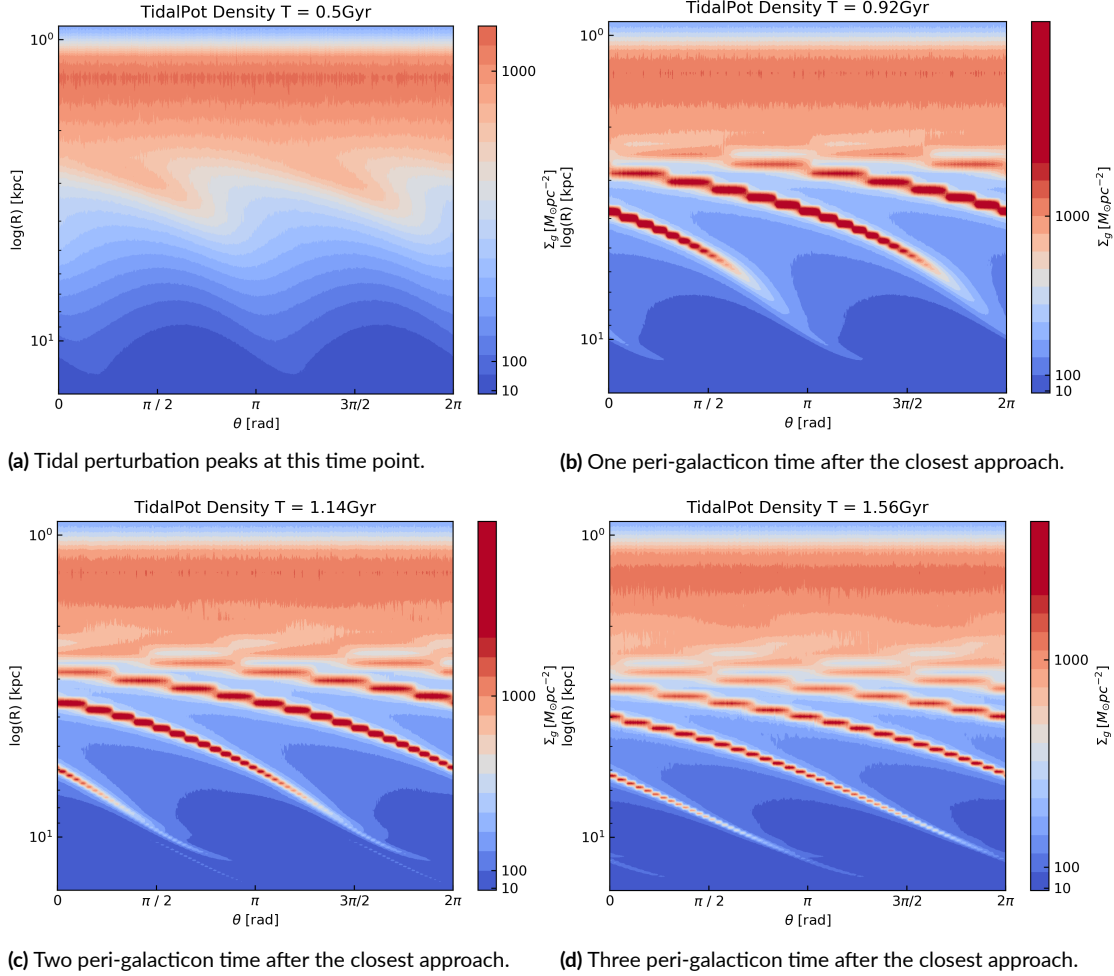


Figure 3.10: This figure shows the logged $r - \theta$ heatmap for tidal interaction. It indicates that the induced spirals are not logarithmic and they are dynamic. Squared patterns are artifacts.

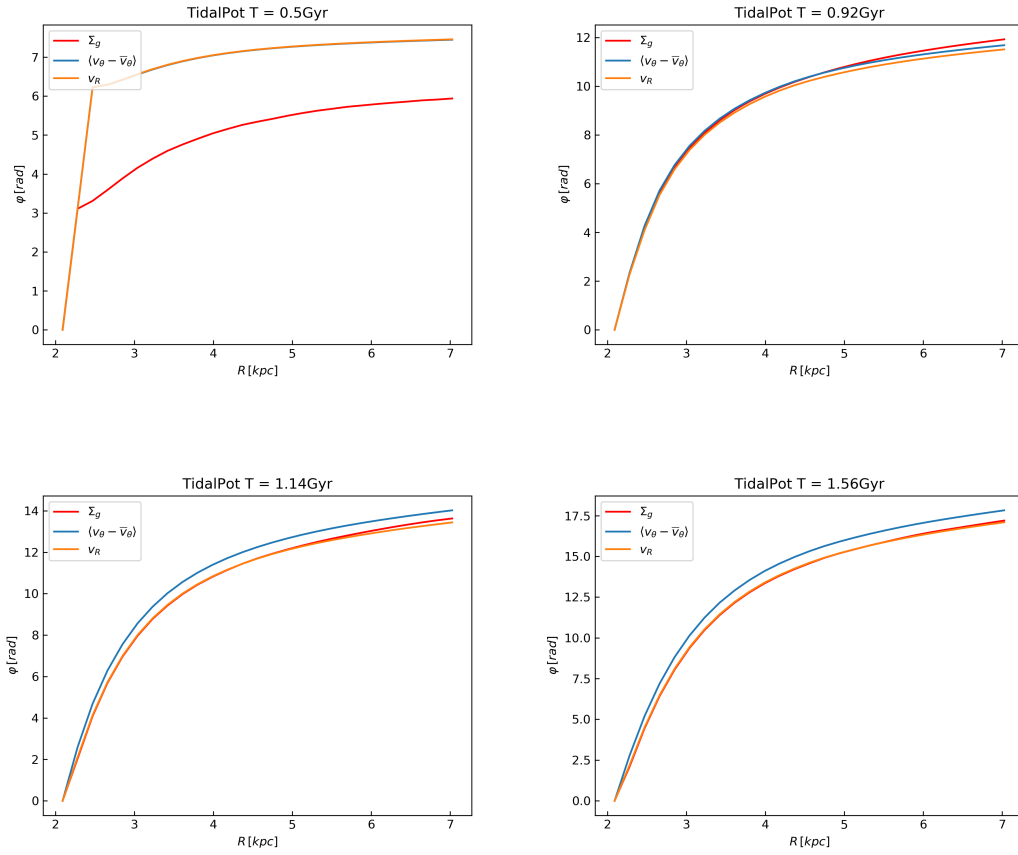


Figure 3.11: This figure shows the phase change and relation between density, azimuthal and radial velocity of gas particles for tidal interaction between disc and the tidal component. A big gap only shows up between phases of density and velocities at large radius at the peak perturbation. The final phase height is time-dependent.

3.4 DENSITY WAVE AND DYNAMIC ARMS

This section present and compare density wave potential and dynamic arm potential impacts on the disc. Figure 3.12 shows the 2D density distribution. For original density wave arms, two grand extended trailing arms could be observed. For the dynamic arms, arms wind up roughly within two rotational periods after the peak perturbation. Though the quick strength change in spirals are not apparent in this plot but in figure 3.13, at $T = 0.37\text{Gyr}$, density wave arms still display strong amplitudes compared with gentle winding arms developed under dynamic arm potential. Both of these two kinds of induced arms are logarithmic as what they are designed and supposed to be, though dynamic arms display more substructures within the central disc.

We then give the offset diagram of density, averaged azimuthal velocity and radial velocity, which is demonstrated by figure 3.14. At the time when the perturbation reaches its peak, both of the two simulation results show density phase and velocity phases tend to diverge with each other at peak perturbation. However, the phase changing speed of density wave arms tend to keep stable while that of the dynamic arms varies and shows a strong time-dependence. Moreover, offset curves of dynamic arms show convergence after the peak perturbation happens. In other words, we could tell how wounded the dynamic arms are according to the offset curve given by the diagram.

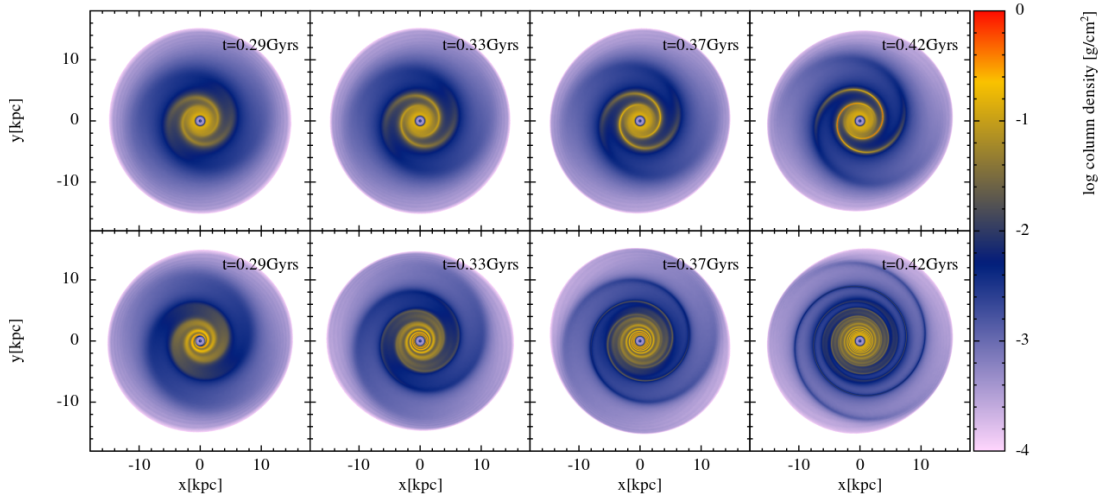


Figure 3.12: The first panel displays the 2D density plot of original density wave arms at $T = 0.29\text{Gyr}$ where the perturbation peaks at and the following time points are one third, two thirds and one orbital period after the peak perturbation. First panel is for density wave arms and the second is for dynamic arms.

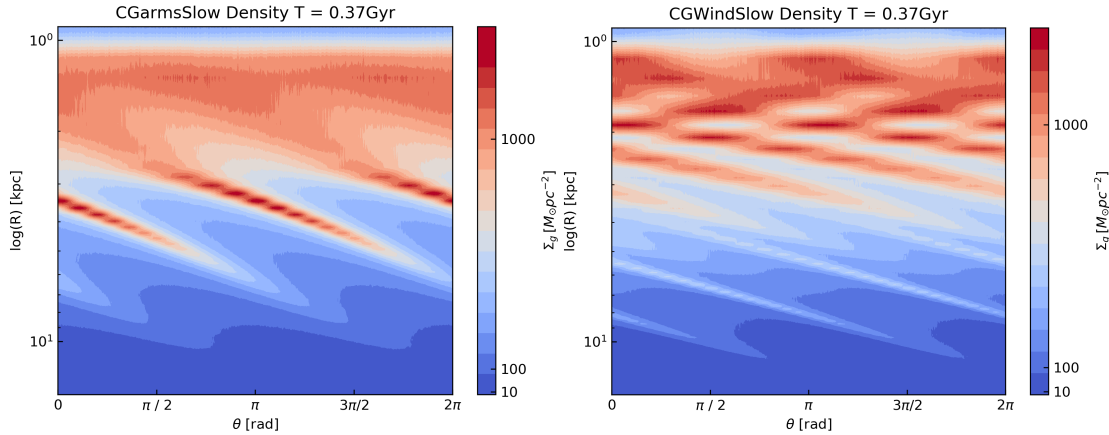


Figure 3.13: This figure shows the logged $r - \theta$ density heatmap of disc response to original density wave arms and dynamic arm potential considering winding and co-rotation effects at $T = 0.37\text{Gyr}$, two thirds of disc orbital period after the peak perturbation.

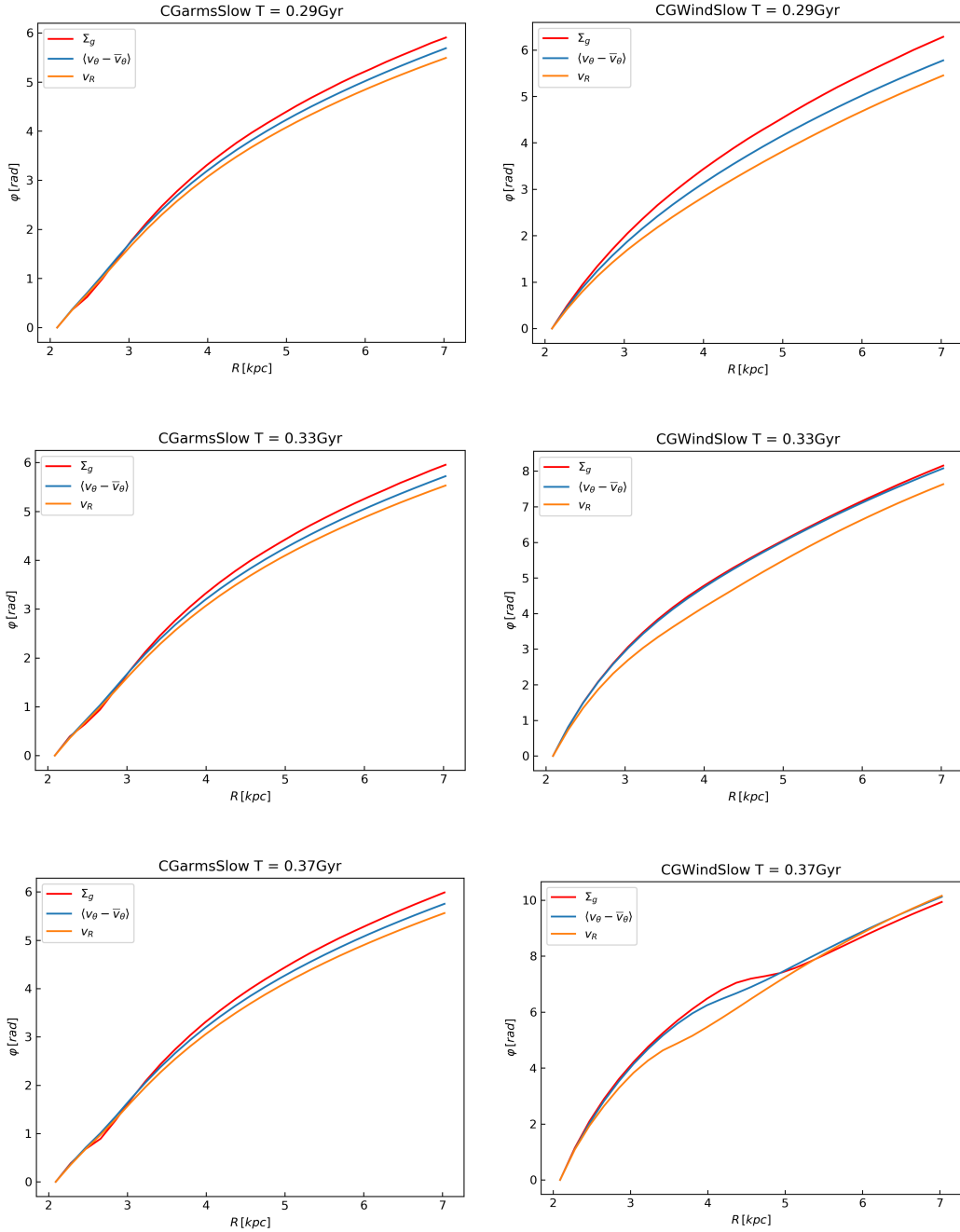


Figure 3.14: This figure shows the offset diagrams of density, averaged azimuthal velocity and radial velocity of original density wave arm potential(first column) and dynamic arm potential(second column) at time where perturbation peaks and the following one third and two thirds disc orbital period after the peak perturbation.

4

Conclusion

We have performed various galactic perturbations including density wave, dynamic arm, tidal interaction and triaxial dark matter halo on high resolution Milky Way like disc and also tested low resolution bulge-free disc as to compare results with past literature. We also have quantitatively analyzed the simulation results using Fourier decomposition and found that,

- Triaxial dark matter halo does not necessarily induce spirals in gaseous galactic disc if its growth is adiabatic enough. Spirals induced by triaxial dark matter halo are very sensitive

to the specific galaxy disc parameter, such as surface density distribution, rotation curve etc.

The only simulation spiral patterns in a Milky Way-like disc is with a triaxility that is not suggested by latest GAIA observational data and it's non-logarithmic, whereas results in previous studies favours that spirals are easy to generate.

- An analysis of the azimuthal locations, the peaks in the velocity and density profiles, phase change of density, averaged azimuthal velocity and radial velocity of density wave arms tend to keep consistent without variation throughout the time but for dynamic arms, phase changes faster as time persists and the three curves tend to reach a convergence that density wave arms offset diagram does not show. For tidal interaction, the offset diagram displays a big gap between velocities and density at peak perturbation but disappears quickly and they show approximately consistent changing speed in phase at each time point after the closest approach. Phases would reach a higher height as time goes by due to the winding effect and show a complete overlap of density and radial velocity. For triaxial dark matter halo, its offset diagram is the only one that shows as a step function in which phases of velocities run faster than that of density. Moreover, in inner disc region, there's an overlap between phases of averaged azimuthal velocity and radial velocity. Since different mechanisms contrast with each other in the offset diagram, we then conclude it could be a diagnostic of the nature of spiral arms in real observed galaxies.

References

- [1] Allan Sandage. *Classification and Stellar Content of Galaxies Obtained from Direct Photography*, 1975 (accessed June, 2020). URL <http://ned.ipac.caltech.edu/level5/Sandageframes.html>.
- [2] NASA ESA. *The Hubble tuning fork classification of galaxies*, 1975 (accessed June, 2020). URL <https://www.spacetelescope.org/images/heic9902o/>.
- [3] Houjun Mo, Frank Van den Bosch, and Simon White. *Galaxy formation and evolution*. Cambridge University Press, 2010.
- [4] Clare Dobbs and Junichi Baba. Dawes review 4: spiral structures in disc galaxies. *Publications of the Astronomical Society of Australia*, 31, 2014.
- [5] Peter MW Kalberla and Jürgen Kerp. The hi distribution of the milky way. *Annual review of astronomy and Astrophysics*, 47:27–61, 2009.
- [6] Eric Chaisson and Stephen McMillan. *Astronomy today*. Pearson/Addison Wesley San Francisco, CA, 2008.
- [7] Massimo Capaccioli. *The winding dilemma*. URL <http://www.federica.unina.it/smfn/physics-of-galaxies/origin-and-stability-spiral-arms/>.
- [8] Alex R Pettitt. The morphology of the milky way. 2014.
- [9] Rahul Shetty and Eve C Ostriker. Global modeling of spur formation in spiral galaxies. *The Astrophysical Journal*, 647(2):997, 2006.
- [10] Kenji Bekki and Kenneth C Freeman. Extended hi spiral structure and the figure rotation of triaxial dark halos. *The Astrophysical Journal Letters*, 574(1):L21, 2002.
- [11] AV Khoperskov, MA Eremin, SA Khoperskov, MA Butenko, and AG Morozov. Dynamics of gaseous disks in a non-axisymmetric dark halo. *Astronomy reports*, 56(1):16–28, 2012.
- [12] Shaoran Hu and Debora Sijacki. Stellar spiral structures in triaxial dark matter haloes. *Monthly Notices of the Royal Astronomical Society*, 461(3):2789–2808, 2016.

- [13] M Dolores Mata-Chávez, Héctor Velázquez, Barbara Pichardo, Octavio Valenzuela, Santi Roca-Fábrega, Héctor Hernández-Toledo, and Erik Aquino-Ortíz. On the dynamical relevance of galaxy spiral arm evolution. i. arm density structure. *The Astrophysical Journal*, 876(1):6, 2019.
- [14] Daniel Price et al. *PHANTOM*, 2020 (accessed June, 2020). URL <https://phantomsph.bitbucket.io>.
- [15] Daniel J Price, James Wurster, Terrence S Tricco, Chris Nixon, Stéven Toupin, Alex Pettitt, Conrad Chan, Daniel Mentiplay, Guillaume Laibe, Simon Glover, et al. Phantom: A smoothed particle hydrodynamics and magnetohydrodynamics code for astrophysics. *Publications of the Astronomical Society of Australia*, 35, 2018.
- [16] Masanori Miyamoto and Ryuzaburo Nagai. Three-dimensional models for the distribution of mass in galaxies. *Publications of the Astronomical Society of Japan*, 27:533–543, 1975.
- [17] Donald P Cox and Gilberto C Gómez. Analytical expressions for spiral arm gravitational potential and density. *The Astrophysical Journal Supplement Series*, 142(2):261, 2002.
- [18] Jason AS Hunt, Jack Hong, Jo Bovy, Daisuke Kawata, and Robert JJ Grand. Transient spiral structure and the disc velocity substructure in gaia dr2. *Monthly Notices of the Royal Astronomical Society*, 481(3):3794–3803, 2018.
- [19] Lorenzo Posti and Amina Helmi. Mass and shape of the milky way’s dark matter halo with globular clusters from gaia and hubble. *Astronomy & Astrophysics*, 621:A56, 2019.
- [20] Walter Dehnen. The effect of the outer lindblad resonance of the galactic bar on the local stellar velocity distribution. *The Astronomical Journal*, 119(2):800, 2000.
- [21] JA Sellwood, Juntai Shen, and Zhi Li. The global stability of m33: still a puzzle. *Monthly Notices of the Royal Astronomical Society*, 486(4):4710–4723, 2019.
- [22] Alar Toomre. What amplifies the spirals. In *Structure and evolution of normal Galaxies*, pages 111–136, 1981.
- [23] JA Sellwood. Bar-halo friction in galaxies. iii. halo density changes. *The Astrophysical Journal*, 679(1):379, 2008.
- [24] Alex R Pettitt, Clare L Dobbs, David M Acreman, and Matthew R Bate. The morphology of the milky way–ii. reconstructing co maps from disc galaxies with live stellar distributions. *Monthly Notices of the Royal Astronomical Society*, 449(4):3911–3926, 2015.